

See discussions, stats, and author profiles for this publication at: <https://www.researchgate.net/publication/332955483>

Numerical dispersion in non-hydrostatic modeling of long-wave propagation

Article · May 2019

DOI: 10.1016/j.ocemod.2019.05.002

CITATIONS

0

READS

87

2 authors:



Linyan Li

University of Hawai'i at Mānoa

8 PUBLICATIONS 78 CITATIONS

SEE PROFILE



Kwok Fai Cheung

University of Hawai'i at Mānoa

155 PUBLICATIONS 3,932 CITATIONS

SEE PROFILE

Some of the authors of this publication are also working on these related projects:



Tsunami survey [View project](#)

Numerical dispersion in non-hydrostatic modeling of long-wave propagation

Linyan Li and Kwok Fai Cheung*

*Department of Ocean and Resources Engineering, University of Hawaii at Manoa, Honolulu, HI
96822, USA*

ABSTRACT

Numerical discretization with a finite-difference scheme is known to introduce frequency dispersion in depth-integrated long-wave models commonly used in tsunami research and hazard mapping. While prior studies on numerical dispersion focused on the linear shallow-water equations, we include the non-hydrostatic pressure and vertical velocity through a Keller box scheme and investigate the properties of the resulting system in relation to a hydrostatic model. Fourier analysis of the discretized governing equations gives rise to a dispersion relation in terms of the time step, grid size, wave direction, and the water-depth parameter. The dispersion relation is illustrated by its lead-order approximation derived from Taylor series expansions as well as numerical experiments involving standing and progressive waves with uniform water depth. Interaction between the spatial discretization and non-hydrostatic terms results in significant reduction of numerical dispersion outside the shallow-water range. Numerical dispersion also decreases for wave propagation oblique to the computational grid due to effective increase in spatial resolution. The time step, which counteracts numerical dispersion from spatial discretization, only has secondary effects within the applicable range of Courant numbers. Since the governing equations of the non-hydrostatic model derived from the Keller box scheme tend to underestimate dispersion in shoaling water, the numerical effects are complementary in producing a solution closer to Airy wave theory. A case study of the 2011 Tohoku tsunami illustrates the grid sensitivity and convergence properties in real-world applications. A properly

* Corresponding author. Tel.: +1-808-956-3485; fax: +1-808-956-3498
E-mail: linyanli@hawaii.edu (L. Li), cheung@hawaii.edu (K.F. Cheung)

selected grid size can achieve accurate description of wave propagation over a wide range of water depth parameters across the ocean.

Keywords: Numerical dispersion, Non-hydrostatic models, Long-wave propagation, Staggered finite-difference scheme, Shallow-water equations, Keller box scheme

1. Introduction

Numerical long-wave models have been an essential tool for tsunami research and hazard mapping. Conventional finite-difference models based on the nonlinear shallow-water equations are the primary choice due to their simple numerical frameworks, low computing costs, and ease of implementation (e.g., Imamura et al. 1988; Kowalik and Bang, 1987; Liu et al. 1995; Titov and Synolakis, 1998). The hydrostatic governing equations describe wave propagation through the shallow-water celerity independent of the wave period. Recent advances in sensor technology have enabled detection of intricate dispersive wave systems even in large catastrophic tsunamis. Hanson and Bowman (2005) and Kulikov (2006) deduced separation of wave components by period in hydrophone and altimetry records of the 2004 Indian Ocean tsunami. Saito et al. (2010) and Yamazaki et al. (2011a) identified strong frequency dispersion in ocean-bottom pressure records of the 2010 Chile and 2011 Tohoku tsunamis. The observations show lagging of short-period components as the tsunami propagates across the open ocean. Near the coast, acoustic Doppler current profiler (ADCP) records have suggested these trailing tsunami waves are the primary energy source for persistent surges and strong currents in insular shelf and reef environments (Bricker et al., 2007; Cheung et al., 2013; Yamazaki et al., 2012a). Recognizing the importance, researchers have been exploring the use of numerical means in shallow-water models as well as high-order properties in Boussinesq-type or non-hydrostatic models to account for frequency dispersion during tsunami propagation.

Discretization of hyperbolic differential equations introduces truncation errors that manifest as dispersion and dissipation in the solution. The Taylor series expansion, which allows detailed

step-by-step analysis of discretization errors, is a classical approach to characterize the property of these numerical artifacts (Abbott et al., 1981; Warming and Hyett, 1974). Trans-oceanic propagation of tsunamis is primarily a linear process because the wave amplitude is small compared to the water depth. Imamura et al. (1988) analyzed the staggered finite-difference scheme with leap-frog time integration for the linear shallow-water equations and showed the grid size and time step can be adjusted to match the lead-order term of the dispersion relation from the Boussinesq-type equations of Peregrine (1967). This approach can numerically describe wave dispersion over a range of water depth parameters around shallow water. Shuto (1991) and Burwell et al. (2007) showed the lead-order approximation can be maintained in varying water depth through adjustment of the grid size for modeling of one-dimensional tsunami propagation. Cho (1995) extended the method to two dimensions by including corrections in the discretized shallow-water equations to mimic the cross-derivative dispersion terms in the Boussinesq-type equations. Instead of adjusting the grid size locally, Cho et al. (2007) and Ha and Cho (2015) introduced variable coefficients in the correction terms to accommodate variation of water depth. Yoon (2002) proposed a variant of the approach by employing a *hidden* grid in the discretized equations with resolution tuned to mimic the lead-order dispersion property at the local water depth. Wang and Liu (2011) adopted this approach to manipulate numerical dispersion for weakly nonlinear and weakly dispersive waves propagating over slowly-varying water depth with a shallow-water model.

More advanced, depth-integrated models can describe dispersion mathematically over a wide range of water depth parameters through the governing equations. One approach is to include high-order terms in the nonlinear shallow-water equations through a Taylor series expansion of the dispersion relation from Airy wave theory (Peregrine, 1967). This gives rise to the Boussinesq-type equations of varying complexity commonly used in modeling of wind-generated waves (e.g., Gobbi et al., 2000; Madsen et al., 1991; Nwogu, 1993; Wei and Kirby, 1995). Boussinesq-type models have also been implemented to account for dispersion in trans-oceanic tsunami propagation (e.g., Horrillo et al., 2006; Kirby et al., 2013; Saito et al., 2014;

Baba et al., 2017). An alternate approach to describe dispersive waves is to directly include the non-hydrostatic pressure and vertical velocity through the Keller box scheme without increasing the order of the governing equations (Stelling and Zijlema, 2003). While a one-layer model is sufficient for tsunami modeling (Yamazaki et al., 2009), additional layers, instead of higher-order derivatives, are used to improve linear and nonlinear properties for modeling of wind-generated waves (e.g., Bai and Cheung, 2013; Smit et al., 2013; Zijlema et al., 2011). The relatively simple numerical framework allows implementation of a two-way grid-nesting scheme for modeling of tsunamis from trans-oceanic propagation to coastal runup (e.g., Yamazaki et al., 2011b; Bai et al., 2018a). The vertical velocity also facilitates modeling of kinematic seafloor deformation to provide a more complete account of tsunami generation and the near-field wave dynamics for inference of earthquake rupture processes (e.g., Yamazaki et al., 2011a, 2018; Lay et al., 2013; Li et al., 2016b; Bai et al., 2018b).

The governing equations of Boussinesq-type and non-hydrostatic models can account for dispersion to varying degree of accuracy in relation to the exact solution from Airy wave theory. While the dispersion relation of the Boussinesq-type equations converges asymptotically at the shallow-water limit, the low-order depth integration accompanying the Keller box scheme leads to slight underestimation of dispersion in shoaling water for the non-hydrostatic approach (Bai et al., 2018c). This is complicated by the discretization scheme, which introduces truncation errors associated with the time step and grid size that interfere with the dispersion property intrinsic to the governing equations. Furthermore, the intrinsic property itself is a mathematical approximation to the physical processes in the ocean. Understanding of the numerical and intrinsic properties is crucial for selection of computational grids that can most appropriately account for physical dispersion and make efficient use of computing resources. However, the truncation error analysis based on the Taylor series expansion becomes very cumbersome with the high-order derivatives in the Boussinesq-type equations. Vitousek and Fringer (2011) decoupled the intrinsic and numerical dispersion by assuming the water depth parameter is small and examined how superposition of numerical dispersion from a shallow-water model to the

intrinsic properties of the one-dimensional Boussinesq and KdV equations would modify internal wave propagation. As the dispersion properties from those governing equations are highly accurate around shallow water, the discretization errors inevitably lead to overestimation of dispersion in the numerical solution. Baba et al. (2017) pointed out the need to use a very small grid size to suppress numerical dispersion in a Boussinesq-type model for computation of tsunami propagation.

Numerical dispersion is present regardless of the governing equations as long as a finite grid size is used in the computation. However, the discretization errors can potentially alleviate the underestimation of dispersion by the governing equations in depth-integrated non-hydrostatic models. The one-layer formulation, which provides the basic building block for multilayer models, serves as a proxy for examination of numerical dispersion in the non-hydrostatic approach. In this study, the non-hydrostatic system of linear governing equations is discretized with a staggered finite difference scheme in the two-dimensional horizontal plane and the Keller box approach in the vertical direction. The non-hydrostatic terms involving the pressure and vertical velocity present a challenge in the Taylor series expansion even though the governing equations remain at first order. The truncation error in the non-hydrostatic pressure is dependent on other variables effectively introducing high-order terms through recursive operations. Numerical dispersion is not directly additive to the intrinsic property of the non-hydrostatic system, as demonstrated in the comparative model study of Li et al. (2016a), and their interaction remains a topic for investigation. The Fourier method provides a straightforward procedure to derive the dispersion relation without expanding the high-order and cross derivative terms as in the Taylor approach. With the dispersion relation expressed in terms of the discretization parameters and aided by numerical experiments and a case study, we explore the coupling between intrinsic and numerical dispersion, the anisotropic propagation property over a two-dimensional computation grid, the use of numerical dispersion to offset errors intrinsic to the governing equations, and the manifestation of numerical dispersion in hydrostatic and non-hydrostatic modeling of tsunamis across the ocean with varying bathymetry.

2. Governing Equations

The non-hydrostatic free surface flow is defined by a Cartesian coordinate system (x, y, z) with the x and y axes in the horizontal plane and the positive z axis pointing upward from the still-water level. Let g denote the acceleration due to gravity, h the water depth, and n the Manning roughness coefficient. The depth-integrated governing equations define conservation of momentum in the x , y , and z directions as well as continuity of flow in the horizontal plane through

$$\frac{\partial U}{\partial t} + U \frac{\partial U}{\partial x} + V \frac{\partial U}{\partial y} = -g \frac{\partial \zeta}{\partial x} - \frac{\partial Q}{\partial x} - \frac{Q}{D} \frac{\partial(\zeta - h)}{\partial x} - n^2 \frac{g}{D^{1/3}} \frac{U \sqrt{U^2 + V^2}}{D} \quad (1)$$

$$\frac{\partial V}{\partial t} + U \frac{\partial V}{\partial x} + V \frac{\partial V}{\partial y} = -g \frac{\partial \zeta}{\partial y} - \frac{\partial Q}{\partial y} - \frac{Q}{D} \frac{\partial(\zeta - h)}{\partial y} - n^2 \frac{g}{D^{1/3}} \frac{V \sqrt{U^2 + V^2}}{D} \quad (2)$$

$$\frac{\partial W}{\partial t} + U \frac{\partial W}{\partial x} + V \frac{\partial W}{\partial y} = \frac{2Q}{D} \quad (3)$$

$$\frac{\partial \zeta}{\partial t} + \frac{\partial(UD)}{\partial x} + \frac{\partial(VD)}{\partial y} = 0 \quad (4)$$

where (U, V, W) is the depth-averaged velocity, ζ is the surface elevation, $D = \zeta + h$ is the flow depth, and Q denotes the depth-averaged non-hydrostatic pressure. The governing equations augment the nonlinear shallow-water system with the non-hydrostatic pressure terms in the horizontal momentum equations (1) and (2) and the addition of the vertical momentum equation (3). The continuity equation (4) remains the same as in the shallow-water equations to ensure conservation of mass.

The Keller box scheme in Stelling and Zijlema (2003) defines the variables at the free surface and seabed. In deriving the horizontal momentum equations (1) and (2), the trapezoidal rule along with the dynamic free surface boundary condition are invoked to approximate the depth-averaged non-hydrostatic pressure as

$$Q = \frac{1}{D} \int_{-h}^{\zeta} q \, dz \approx \frac{1}{2} (q_{\zeta} + q_b) = \frac{1}{2} q_b \quad (5)$$

where q_b and q_ζ denote the non-hydrostatic pressure at the bottom and free surface. The same rule integrates the vertical velocity w to give the depth-averaged W in the momentum equation (3) as

$$W = \frac{1}{D} \int_{-h}^{\zeta} w \, dz \approx \frac{1}{2} (w_\zeta + w_b) \quad (6)$$

in which the vertical velocity at the free surface and bottom are given by the kinematic boundary conditions as

$$w_\zeta = \frac{\partial \zeta}{\partial t} + U \frac{\partial \zeta}{\partial x} + V \frac{\partial \zeta}{\partial y} \quad \zeta \quad z = \quad (7)$$

$$w_b = -U \frac{\partial h}{\partial x} - V \frac{\partial h}{\partial y} \quad z = -h \quad (8)$$

For a linear variation of the vertical velocity over depth, the non-hydrostatic pressure should follow a quadratic distribution (Jeschke et al., 2017), but is also approximated as linear in the depth integration (5) following the Keller box scheme. This approximation leads to slight underestimation of dispersion in shoaling water with non-asymptotic convergence at the shallow-water limit even for a multi-layer model (Bai et al., 2018c).

Dispersion analysis is based on linear wave propagation over uniform water depth in the absence of bottom friction. The x , y , and z momentum equations and the continuity equation become

$$\frac{\partial U}{\partial t} = -g \frac{\partial \zeta}{\partial x} - \frac{\partial Q}{\partial x} \quad (9)$$

$$\frac{\partial V}{\partial t} = -g \frac{\partial \zeta}{\partial y} - \frac{\partial Q}{\partial y} \quad (10)$$

$$\frac{\partial W}{\partial t} = \frac{2Q}{h} \quad (11)$$

$$\frac{\partial \zeta}{\partial t} + h \frac{\partial U}{\partial x} + h \frac{\partial V}{\partial y} = 0 \quad (12)$$

The governing equations include terms of up to first order, but implicitly contain a third-order dispersion term as inferred from their equivalent Boussinesq form (Bai et al., 2018c). There are

four equations and five unknowns, U , V , W , ζ , and Q , in the non-hydrostatic system.

Conservation of mass requires

$$\frac{\partial U}{\partial x} + \frac{\partial V}{\partial y} + \frac{\partial w}{\partial z} = 0 \quad (13)$$

in which

$$\frac{\partial w}{\partial z} = \frac{2W}{h} \quad (14)$$

for a linear profile of w over the water column. This fifth equation links the three velocity components and closes the system of equations for a solution. The governing equations (9) - (13) already include the discretization in the vertical direction through the depth integration (5) and (6) and the accompanying approximation of a linear profile in the Keller box scheme with equation (14).

Figure 1 shows the staggered finite-difference grid for the discretization in the two-dimensional horizontal plane. The domain is divided into computational cells of dimensions Δx and Δy in the x and y directions. The horizontal velocity components U and V are defined at the cell interfaces $(i \pm 1/2, j)$ and $(i, j \pm 1/2)$ and the surface elevation ζ , vertical velocity W , and non-hydrostatic pressure Q at the cell center (i, j) . The linearized governing equations (9) to (13) are discretized as

$$\frac{U_{i+1/2,j}^{m+1} - U_{i+1/2,j}^m}{\Delta t} + g \frac{\zeta_{i+1,j}^m - \zeta_{i,j}^m}{\Delta x} + \frac{Q_{i+1,j}^{m+1} - Q_{i,j}^{m+1}}{\Delta x} = 0 \quad (15)$$

$$\frac{V_{i,j+1/2}^{m+1} - V_{i,j+1/2}^m}{\Delta t} + g \frac{\zeta_{i,j+1}^m - \zeta_{i,j}^m}{\Delta y} + \frac{Q_{i,j+1}^{m+1} - Q_{i,j}^{m+1}}{\Delta y} = 0 \quad (16)$$

$$\frac{W_{i,j}^{m+1} - W_{i,j}^m}{\Delta t} - \frac{2Q_{i,j}^{m+1}}{h} = 0 \quad (17)$$

$$\frac{\zeta_{i,j}^{m+1} - \zeta_{i,j}^m}{\Delta t} + h \frac{U_{i+1/2,j}^{m+1} - U_{i-1/2,j}^{m+1}}{\Delta x} + h \frac{V_{i,j+1/2}^{m+1} - V_{i,j-1/2}^{m+1}}{\Delta y} = 0 \quad (18)$$

$$\frac{U_{i+1/2,j}^{m+1} - U_{i-1/2,j}^{m+1}}{\Delta x} + \frac{V_{i,j+1/2}^{m+1} - V_{i,j-1/2}^{m+1}}{\Delta y} + \frac{2W_{i,j}^{m+1}}{h} = 0 \quad (19)$$

where the superscript m denotes the current time step and Δt is the time step size. As far as the hydrostatic system is concerned, the first-order time integration is explicit for the flow velocity in the horizontal momentum equations (15) and (16) and implicit for the surface elevation in the continuity equation (18). The use of the horizontal velocity at $(m+1)$ in the time integration of the surface elevation introduces second-order truncation properties identical to the commonly-used leap-frog scheme (see Appendix A). While the spatial derivatives are approximated by second-order central differences, the semi-implicit time integration stabilizes the computation (Kowalik and Murty, 1993). The leapfrog scheme, which is explicit and second order, can alternatively pair with the second-order spatial discretization to integrate the solution in time with the same order of accuracy (Imamura et al., 1988; Liu et al. 1995; Zijlema et al. 2011; Smit et al., 2014).

The non-hydrostatic pressure in the horizontal momentum equations (15) and (16) is defined at the new time step $(m+1)$ and is solved implicitly from a Poisson-type equation assembled from the mass conservation (19). A semi-implicit solution approach evaluates the hydrostatic and non-hydrostatic components in two steps (Chorin, 1968). Integration of equations (15) and (16), with non-hydrostatic pressure terms omitted, provides an initial estimate for the horizontal velocity (U , V) at $(m+1)$. Substitution of U , V and W , expressed in terms of the non-hydrostatic pressure Q from the momentum equations (15) - (17), into the mass conservation (19) gives a matrix equation of Poisson-type as

$$\begin{aligned}
& -\frac{\Delta t}{\Delta x^2} Q_{i-1,j}^{m+1} - \frac{\Delta t}{\Delta x^2} Q_{i+1,j}^{m+1} - \frac{\Delta t}{\Delta y^2} Q_{i,j-1}^{m+1} - \frac{\Delta t}{\Delta y^2} Q_{i,j+1}^{m+1} + \left(\frac{2\Delta t}{\Delta x^2} + \frac{2\Delta t}{\Delta y^2} + \frac{4\Delta t}{h^2} \right) Q_{i,j}^{m+1} \\
& = -\frac{U_{i+1/2,j}^{*m+1} - U_{i-1/2,j}^{*m+1}}{\Delta x} - \frac{V_{i,j+1/2}^{*m+1} - V_{i,j-1/2}^{*m+1}}{\Delta y} - \frac{2W_{i,j}^m}{h}
\end{aligned} \tag{20}$$

where the asterisk (*) denotes initial estimates of the horizontal velocity components from the hydrostatic step. The matrix equation leads to an implicit solution for the non-hydrostatic pressure Q at $(m+1)$. The velocity (U , V , W) is then updated from integration of the non-hydrostatic terms in the momentum equations (15) - (17) and ζ from the continuity equation (18) before proceeding to the next time step.

3. Fourier and Taylor Expansions

The Fourier expansion, which has been a standard approach in deriving dispersion relations for governing equations of free surface flow, is implemented here to study the propagation property of the non-hydrostatic model formulated in Section 2. The discretization transforms the governing differential equations into a system of algebraic equations, which must be satisfied by each frequency component in the expansion. The resulting eigenvalue matrix links the wave frequency and number as well as the discretization parameters in a dispersion relation. This analytical technique has also been used to study numerical dispersion and stability in shallow-water models (e.g., Foreman, 1984; Leendertse, 1967; Sankaranarayanan and Spaulding, 2003). Its extension to the non-hydrostatic system involves two additional variables with the rank of the eigen-value matrix increased by two. The resulting dispersion relation expressed in trigonometric functions can in turn be expanded by Taylor series to illustrate systematically the order of truncation errors as in the conventional approach for the shallow-water models (Imamura et al., 1988).

We consider a system of regular progressive waves on water of uniform water depth for derivation of the dispersion relation. The surface elevation ζ , flow velocity (U , V , W), and non-hydrostatic pressure Q are expressed as discrete Fourier modes over the staggered finite difference grid in Figure 1 as

$$\zeta_{i,j}^m = \zeta_o e^{i(ik_x \Delta x + jk_y \Delta y - m\omega \Delta t)} \quad (21)$$

$$U_{i\pm 1/2,j}^m = U_o e^{i((i\pm 1/2)k_x \Delta x + jk_y \Delta y - m\omega \Delta t)} \quad (22)$$

$$V_{i,j\pm 1/2}^m = V_o e^{i(ik_x \Delta x + (j\pm 1/2)k_y \Delta y - m\omega \Delta t)} \quad (23)$$

$$W_{i,j}^m = W_o e^{i(ik_x \Delta x + jk_y \Delta y - m\omega \Delta t)} \quad (24)$$

$$Q_{i,j}^m = Q_o e^{i(ik_x \Delta x + jk_y \Delta y - m\omega \Delta t)} \quad (25)$$

where the subscript o indicates the amplitude of the variables, $i = \sqrt{-1}$ is an imaginary number, ω is the wave frequency, and k_x and k_y are the x and y components of the wave number vector \vec{k} such that $k^2 = k_x^2 + k_y^2$. While the wave number is real, the angular frequency can be complex with real and imaginary parts representing dispersion and dissipation in the discretization scheme (Leendertse, 1967).

The discrete Fourier modes (21) - (25) represent a general analytical solution to the linear non-hydrostatic system. Their substitution into the discretized governing equations (15) - (19) gives

$$\frac{U_o e^{i(k_x \Delta x / 2)} (\lambda - 1)}{\Delta t} + g \frac{\zeta_o (e^{i(k_x \Delta x)} - 1)}{\Delta x} + \frac{Q_o (e^{i(k_x \Delta x)} - 1) \lambda}{\Delta x} = 0 \quad (26)$$

$$\frac{V_o e^{i(k_y \Delta y / 2)} (\lambda - 1)}{\Delta t} + g \frac{\zeta_o (e^{i(k_y \Delta y)} - 1)}{\Delta y} + \frac{Q_o (e^{i(k_y \Delta y)} - 1) \lambda}{\Delta y} = 0 \quad (27)$$

$$\frac{W_o (\lambda - 1)}{\Delta t} - \frac{2Q_o \lambda}{h} = 0 \quad (28)$$

$$\frac{\zeta_o (\lambda - 1)}{\Delta t} + h \frac{U_o [2i \sin(k_x \Delta x / 2)] \lambda}{\Delta x} + h \frac{V_o [2i \sin(k_y \Delta y / 2)] \lambda}{\Delta y} = 0 \quad (29)$$

$$\frac{U_o [2i \sin(k_x \Delta x / 2)] \lambda}{\Delta x} + \frac{V_o [2i \sin(k_y \Delta y / 2)] \lambda}{\Delta y} + \frac{2W_o \lambda}{h} = 0 \quad (30)$$

where $\lambda = e^{-i\omega \Delta t}$ denotes the eigenvalue. The homogeneous system of equations can be written in matrix form as

$$\begin{pmatrix}
g \frac{2i \sin(k_x \Delta x / 2)}{\Delta x} & \frac{\lambda - 1}{\Delta t} & 0 & 0 & \frac{i \sin(k_x \Delta x / 2) \lambda}{\Delta x} \\
g \frac{2i \sin(k_y \Delta y / 2)}{\Delta y} & 0 & \frac{\lambda - 1}{\Delta t} & 0 & \frac{i \sin(k_y \Delta y / 2) \lambda}{\Delta y} \\
0 & 0 & 0 & \frac{\lambda - 1}{\Delta t} & -\frac{\lambda}{h} \\
\frac{\lambda - 1}{\Delta t} & h \frac{2i \sin(k_x \Delta x / 2) \lambda}{\Delta x} & h \frac{2i \sin(k_y \Delta y / 2) \lambda}{\Delta y} & 0 & 0 \\
0 & \frac{i \sin(k_x \Delta x / 2) \lambda}{\Delta x} & \frac{i \sin(k_y \Delta y / 2) \lambda}{\Delta y} & \frac{\lambda}{h} & 0
\end{pmatrix}
\begin{pmatrix}
\zeta_o \\
U_o \\
V_o \\
W_o \\
Q_o
\end{pmatrix} = 0 \quad (31)$$

in which the grid size and time step function as free parameters modulating the numerical properties. The eigenvalue is equivalent to an amplification factor in the wave propagation processes and its modulus must be less than or equal to one for a stable numerical solution.

The matrix equation (31) represents propagation of a system of regular waves through the staggered finite-difference grid in Figure 1. A non-trivial solution requires the determinant of the matrix to be zero giving rise to

$$\frac{\lambda^2 (1 - \lambda) h^2}{\Delta t^3} \left\{ \frac{h^2 [1 - \cos(k_x \Delta x)]}{2 \Delta x^2} + \frac{h^2 [1 - \cos(k_y \Delta y)]}{2 \Delta y^2} + 1 \right\} [\lambda^2 + 2(a - 1)\lambda + 1] = 0 \quad (32)$$

in which

$$a = \frac{2gh\Delta t^2 \Delta y^2 [1 - \cos(k_x \Delta x)] + 2gh\Delta t^2 \Delta x^2 [1 - \cos(k_y \Delta y)]}{2\Delta x^2 \Delta y^2 + h^2 \Delta y^2 [1 - \cos(k_x \Delta x)] + h^2 \Delta x^2 [1 - \cos(k_y \Delta y)]} \quad (33)$$

and is always greater than zero. The system has three eigenvalues

$$\lambda = \left\{ 1, (1 - a) \pm \sqrt{a(a - 2)} \right\} \quad (34)$$

The eigenvalue of $\lambda = 1$ is equivalent to $\omega = 0$ denoting a steady flow. The remaining two eigenvalues $\lambda = (1 - a) \pm \sqrt{a(a - 2)}$ must be complex to represent wave propagation. This implies $a < 2$, leading to

$$\lambda = (1 - a) \pm i\sqrt{a(2 - a)} \quad (35)$$

Both eigenvalues have a modulus of one indicating the discretization scheme is neutrally stable.

As a result, the eigenvalue $\lambda = e^{-i\omega\Delta t}$ can alternatively be expressed as

$$\lambda = \cos(\omega\Delta t) - i \sin(\omega\Delta t) \quad (36)$$

Comparison with equation (35) gives $\cos(\omega\Delta t) = (1 - a)$ or

$$\cos(\omega\Delta t) = 1 - \frac{2gh\Delta t^2\Delta y^2[1 - \cos(k_x\Delta x)] + 2gh\Delta t^2\Delta x^2[1 - \cos(k_y\Delta y)]}{2\Delta x^2\Delta y^2 + h^2\Delta y^2[1 - \cos(k_x\Delta x)] + h^2\Delta x^2[1 - \cos(k_y\Delta y)]} \quad (37)$$

which links the frequency and wave number in the form of a dispersion relation and accounts for the effects of numerical discretization as a phase error through the time step parameter $\omega\Delta t$ and the grid size parameters $k_x\Delta x$ and $k_y\Delta y$.

Setting $\Delta x = \Delta y$ simplifies Equation (37) to illustrate the fundamental processes and provide general guidance for selection of grid spacing in numerical modeling. The resulting dispersion relation for the non-hydrostatic model can be expressed in terms of the Courant number $Cr = \sqrt{gh}\Delta t / \Delta x$ to give the celerity as

$$c = \sqrt{gh} \frac{1}{Cr(k\Delta x)} \arccos \left\{ 1 - \frac{2Cr^2(k\Delta x)^2 [2 - \cos(\sqrt{\alpha}k\Delta x) - \cos(\sqrt{1-\alpha}k\Delta x)]}{2(k\Delta x)^2 + (kh)^2 [2 - \cos(\sqrt{\alpha}k\Delta x) - \cos(\sqrt{1-\alpha}k\Delta x)]} \right\} \quad (38)$$

where kh is the water depth parameter and $\alpha = k_x^2 / k^2$ varies from 1 to 0 for wave directions between 0 to 90° from the x axis. At the shallow-water limit with $kh = 0$, the dispersion relation (38) reduces to

$$c = \sqrt{g} \frac{h}{Cr(k\Delta x)} \arccos \left\{ 1 - Cr^2 [2 - \cos(\sqrt{\alpha}k\Delta x) - \cos(\sqrt{1-\alpha}k\Delta x)] \right\} \quad (39)$$

for the hydrostatic model. Numerical dispersion is a function of the spatial and temporal discretization parameters denoted by $k\Delta x$ and Cr . The theoretical upper bound of $k\Delta x$ is π analogous to the Nyquist frequency in resolving a harmonic, while Cr is subject to the stability condition of $a < 2$ such that the modulus of the eigenvalues is equal to or less than 1. From equation (33), the stability condition gives rise to $Cr < 1$ with $(k_x\Delta x, k_y\Delta y) = (\pi, 0)$ or $(0, \pi)$ for

wave propagation along a principal axis and $Cr < 1/\sqrt{2}$ with $(k_x\Delta x, k_y\Delta y) = (\pi, \pi)$ for propagation along the diagonal as illustrated by the effective grid spacing in Figure 1.

The dispersion relation (38) is the exact solution to the discretized governing equations (15) to (19), but does not fully reveal the interplay between the depth and discretization parameters. To illustrate the lead-order properties, we expand the cosine functions in equation (37) about $k_x\Delta x = 0$, $k_y\Delta y = 0$, and $\omega\Delta t = 0$ by Taylor series. With $\Delta x = \Delta y$, we have

$$c^2 - \frac{c^4}{12}(k\Delta t)^2 = gh \frac{1 - \frac{1}{12}(k\Delta x)^2 + \frac{k_x^2 k_y^2}{6k^2} \Delta x^2}{1 + \frac{1}{4}(kh)^2 \left[1 - \frac{1}{12}(k\Delta x)^2 + \frac{k_x^2 k_y^2}{6k^2} \Delta x^2 \right]} + O(\Delta x^4, \Delta t^4) \quad (40)$$

where truncation errors of fourth or higher order are grouped under $O(\Delta x^4, \Delta t^4)$. The relation can be rewritten with the c^4 term on the left-hand side as truncation errors as

$$c^2 = gh \frac{1 - \frac{1}{12}(k\Delta x)^2 + \frac{k_x^2 k_y^2}{6k^2} \Delta x^2}{1 + \frac{1}{4}(kh)^2 \left[1 - \frac{1}{12}(k\Delta x)^2 + \frac{k_x^2 k_y^2}{6k^2} \Delta x^2 \right]} + O(\Delta x^4, \Delta t^2) \quad (41)$$

Substituting equation (41) into the c^4 term in equation (40) and neglecting fourth and higher-order terms in $k\Delta x$ and $\omega\Delta t$, we have the lead-order dispersion relation

$$c = \sqrt{gh} \left\{ \frac{1}{1 + \frac{1}{4}(kh)^2} - \frac{\frac{1}{12}(k\Delta x)^2 (\beta - Cr^2)}{\left[1 + \frac{1}{4}(kh)^2 \right] \left[1 + \frac{1}{4}(kh)^2 - \frac{\beta}{24}(kh)^2 (k\Delta x)^2 \right]} \right\}^{1/2} \quad (42)$$

where $\beta = 1 - 2k_x^2 k_y^2 / k^4$ varies between 1 and 0.5 for wave propagating along the principal axes and the diagonal at 45° . Introducing $\Delta x^2 = \gamma h^2 + gh\Delta t^2$, which is a generalization from Imamura et al. (1988), gives

$$c = \sqrt{gh} \left\{ \frac{1 + \left[\frac{1}{4} - \frac{\gamma(\beta - Cr^2)}{12(1 - Cr^2)} \right] (kh)^2 - \frac{\gamma\beta}{24(1 - Cr^2)} (kh)^4}{1 + \frac{1}{2}(kh)^2 + \left[\frac{1}{16} - \frac{\gamma\beta}{24(1 - Cr^2)} \right] (kh)^4 - \frac{\gamma\beta}{96(1 - Cr^2)} (kh)^6} \right\}^{1/2} \quad (43)$$

312 The parameter $\gamma = (\Delta x^2 - gh\Delta t^2)/h^2$ combines the effects of the grid size, time step, and water
 313 depth to indicate the level of numerical dispersion relative to the intrinsic property from the
 314 continuous governing equations (9) - (13).

315 **4. Dispersion Relations**

316 Both dispersion relations (38) and (42) give the celerity in terms of the water depth parameter
 317 kh , discretization parameters $k\Delta x$ and Cr , and the relative wave direction α or β ; the latter, lead-
 318 order form provides a framework to examine the asymptotic properties and demonstrate the
 319 inter-relationship among the parameters. In this section, we focus on the dispersion properties of
 320 the non-hydrostatic model with respect to Airy wave theory and use results from the shallow-
 321 water and Boussinesq-type equations as baselines for comparison. Introduction of the combined
 322 grid size, time step, and water depth parameter γ in the dispersion relation (43) allows elucidation
 323 of the convergence properties and provides guidance for practical application in tsunami
 324 modeling.

325 *4.1 Asymptotic properties*

326 The lead-order approximation (42) is derived from Taylor series expansions of the
 327 trigonometric functions in the dispersion relation (38) and is valid for small values of the
 328 discretization parameters for examination of the asymptotic properties. In the absence of
 329 discretization errors, numerical dispersion and wave directionality vanish. The expression
 330 reduces to

$$331 \quad c = \sqrt{gh} \left[1 + \frac{1}{4} (kh)^2 \right]^{-1/2} \quad (44)$$

332 which is the intrinsic dispersion relation of the continuous governing equations (9) - (13).
 333 Equation (44) has the same structure as the dispersion relation of the Boussinesq-type equations
 334 from Peregrine (1967), but has a coefficient of 1/4 instead of 1/3 for the water depth parameter.
 335 The coefficient 1/4 is carried over from the dispersion term of the governing equations of the

non-hydrostatic system in Boussinesq form (Bai et al., 2018c). A comparison between equations (44) and (43) shows the discretization augments the order of the dispersion relation from a $[0, 2]$ to a $[4, 6]$ rational function along with introduction of the parameter γ for model optimization or error assessment.

Numerical dispersion in shallow-water models has been studied extensively. Here we seek to illustrate the property in terms of the water depth parameter. When $kh = 0$, the non-hydrostatic terms in the governing equations vanish and the dispersion relation (42) reduces to

$$c = \sqrt{g} \left[h \left(1 - \frac{\beta}{12} (k\Delta x)^2 + \frac{1}{12} Cr^2 (k\Delta x)^2 \right) \right]^{1/2} \quad (45)$$

Setting $\beta = 1$ results in the lead-order dispersion relation for wave propagation along a principal axis. The resulting expression is identical to that derived by Imamura et al. (1988) due to the use of the same staggered finite difference grid and the comparable time integration schemes to second order (see Appendix A). Substitution of $\Delta x^2 = \gamma h^2 + gh\Delta t^2$ yields

$$c = \sqrt{gh} \left[1 - \frac{\gamma}{12} (kh)^2 \right]^{1/2} \quad (46)$$

where kh is reintroduced into the dispersion relation of the hydrostatic model to account for depth-dependence of discretization errors. Imamura et al. (1988) showed a value of $\gamma = 4$ gives rise to

$$c = \sqrt{gh} \left[1 - \frac{1}{3} (kh)^2 \right]^{1/2} \quad (47)$$

which is the lead-order expansion of the dispersion relation from the Boussinesq-type equations of Peregrine (1967). A value of $\gamma = 3$ results in a coefficient of $1/4$ for the depth parameter, providing a lead-order approximation to the intrinsic dispersion relation (44) of the non-hydrostatic system.

The propagation property in the governing equations boils down to the coefficient in the intrinsic dispersion relation. The Boussinesq-type approach yields a coefficient of $1/3$ with accurate results around the shallow-water range and asymptotic convergence to Airy wave theory

at $kh = 0$. The coefficient $1/4$, which results from the linear non-hydrostatic pressure profile in the depth integration (5), leads to slight underestimation of the dispersion in shoaling water, but better agreement with Airy wave theory toward deep water (Bai et al., 2018c). An assumption of a quadratic profile for the non-hydrostatic pressure can produce a coefficient of $1/3$ equivalent to the Boussinesq-type equations (Jeschke et al., 2017). Discretization errors are always present in the numerical solution even with an accurate account of dispersion from the governing equations. A small grid size can help alleviate the numerical artifacts, but will increase the computing cost and limit the model application. The slightly weaker dispersion intrinsic in the governing equations of the non-hydrostatic model provides an opportunity to accommodate discretization errors in matching the numerical solution with Airy wave theory.

4.2 Inter-relationship among parameters

The lead-order dispersion relation (42) shows the intrinsic property from the governing equations and its influence on the numerical contribution in separate terms. The underlying expansion stands out the role of each parameter and its inter-relationship with the others. The water depth parameter kh lowers the celerity through intrinsic dispersion and interacts with the spatial and temporal discretizations to modulate the numerical property. While the upper bound of the grid size parameter $k\Delta x$ is π , the practical maximum is around one for resolution of a wavelength with at least six computational cells, such that the denominator of the numerical dispersion term is always positive. The wave direction parameter β has a range of 0.5 to 1.0 and the Courant number Cr must be less than $1/\sqrt{2}$ for wave propagation over a two-dimensional grid. The positive numerator indicates the primary role of the temporal discretization in increasing the celerity while reducing numerical dispersion. In contrast, the parameter $k\Delta x$ facilitates reduction of the celerity through the numerator and denominator of the numerical dispersion term. The complementary effects of kh and $k\Delta x$ provides the basis for the use of spatial discretization errors to mimic dispersion in numerical wave models. It is important to note

that the presence of kh in the denominator indicates reduction of discretization errors with increasing water depth or intrinsic dispersion.

The exact dispersion relation (38) describes the celerity without assuming small values of the discretization parameters to aid interpretation of the property over the full range. Figure 2a plots the celerity over $k\Delta x$ and Cr with the propagation direction along the x axis. The depth parameter kh from 0 to 0.6 is most relevant to tsunami modeling (Bai and Cheung, 2016a). The celerity decreases and dispersion increases with kh and $k\Delta x$, but vice versa with Cr . The Courant number plays a secondary role in counteracting numerical dispersion because of its coupling with $k\Delta x$ resulting in a combined fourth order term as shown in the lead-order approximation (42). Oblique wave propagation also reduces numerical dispersion. Figure 2b demonstrates the increased celerity with an oblique wave direction of 45° from the x axis. The lead-order dispersion relation (42) can provide an insight into the mechanism. The parameter β can be incorporated into the discretization parameter as $k(\sqrt{\beta}\Delta x)$ to denote an effective grid size in terms of the wave direction relative to the x axis. Since $\beta \leq 1$, the decrease in effective grid spacing reduces numerical dispersion for oblique wave propagation. Turning the waves to 45° with $\beta = 1/2$ has the same effects on the celerity as a reduction of the grid size by a factor of $1/\sqrt{2}$ as illustrated geometrically in Figure 1. The results also show increased influence of Cr at the smaller value of $\beta = 0.5$ as indicated in the lead-order dispersion relation.

It is useful to investigate the interplay between intrinsic and numerical dispersion in matching Airy wave theory. We consider waves propagating along the x axis for illustration. The concept of effective grid spacing can be applied to infer numerical dispersion for oblique wave directions. Figure 3 plots the celerity from the dispersion relation (38) normalized by the exact solution from Airy wave theory over $k\Delta x$ and Cr . The celerity reduction or numerical dispersion is most prominent in the absence of intrinsic dispersion at $kh = 0$. The governing equations of the hydrostatic and non-hydrostatic models give higher predictions of the celerity in relation to Airy wave theory when $kh > 0$. Numerical dispersion can offset the overestimation in matching the exact solution through a combination of spatial and temporal discretization errors. The effects,

however, are relatively mild and insensitive at small values of $k\Delta x$. The hydrostatic model requires a grid size of $k\Delta x > 0.6$ to achieve the correct dispersion property outside the shallow-water range. A slightly larger grid size is needed to counter the effects of temporal discretization. Within the applicable range of $k\Delta x$, numerical dispersion alone is not sufficient to match Airy wave theory above $kh \approx 0.5$. Inclusion of the non-hydrostatic terms in the governing equations alleviates this requirement and enables achievement of proper dispersion within the range of $k\Delta x$ for accurate resolution of tsunami waves.

4.3 Convergence with grid size and water depth

A tsunami consists of a range of harmonics associated with the complexity of the bathymetry at the source and the seafloor deformation from earthquake rupture. Recent advances in imaging techniques using combinations of global seismic waves, region GPS observations, near-field tsunami waveforms, and coastal runup measurements have led to unprecedented details in source models for inference of earthquake rupture processes (Lay, 2018). Since the initial harmonic components of the tsunami are defined spatially in terms of the wavelength at the source, dispersion is key to reproduction of the wave period distribution across the ocean as well as multi-scale resonance and impact near the coast. It is therefore important for a numerical model to match the dispersion relation from Airy wave theory over an appropriate range of water depth parameters beyond the shallow-water range for practical applications.

The hydrostatic model, in which numerical dispersion has been extensively studied, provides a baseline for comparison. Figure 4a plots the normalized celerity from the dispersion relation (39) as a function of kh , reintroduced by substitution of $\Delta x^2 = \gamma h^2 + gh\Delta t^2$. Since the time step size plays a secondary role in numerical dispersion, we assign a small value of $Cr = 0.01$ to focus on the effects of spatial discretization. With $\Delta t \rightarrow 0$, the combined grid size and depth parameter $\gamma = (\Delta x/h)^2$ relates the numerical component of the model celerity versus the intrinsic component from the governing equations in defining the propagation property across the ocean. The results illustrate strong dependence of numerical dispersion on γ and kh . At $\gamma = 0$, the lack of dispersion

in the shallow-water equations results in substantial overestimation of the celerity with increasing kh . Increasing the value of γ leads to numerical dispersion that in turn reduces the celerity. A value of $\gamma = 4$, which reproduces the lead-order term of the dispersion relation from the Boussinesq-type equations of Peregrine (1967), provides a very good approximation of the celerity from Airy wave theory around shallow water. The results show a 0.53% error at $kh = 0.6$ around the upper limit of the tsunami range. The celerity is quite sensitive to γ , especially outside shallow water. Through local adjustment of the grid size with water depth, Wang and Liu (2011) managed to mimic the lead-order dispersion property over varying bathymetry by maintaining $\gamma = 4$ using a hydrostatic model.

The discretization errors can similarly be tuned to augment the dispersion relation (38) of the non-hydrostatic model for improved wave propagation characteristics as shown in Figure 4b. A large value of $\gamma = 4$ results in excess numerical dispersion leading to underestimation of the celerity even within the shallow-water range. Reducing γ leads to increase of the celerity, but at a lower rate over a smaller range comparing to the hydrostatic model results in Figure 4a. In comparison to Airy wave theory, the intrinsic dispersion relation at $\gamma = 0$ slightly underestimates dispersion for $kh < 2.4$. A value of $\gamma = 0.8$ introduces the right amount of numerical dispersion to offset the underestimation and reproduces the celerity up to $kh = 0.6$ and 1.2 with less than 0.13% and 0.77% error comparing to Airy wave theory. The resulting dispersion relation follows closely the Boussinesq-type equations of Peregrine (1967) for tsunami modeling and has slightly better performance over most of the intermediate depth range. Tuning of numerical dispersion in the non-hydrostatic model might provide a computationally efficient alternative, instead of additional layers, for modeling of surf-zone processes involving wind-generated waves. The governing equations account for a significant portion of physical dispersion and reduce the effects of spatial discretization with increasing kh . Numerical dispersion also becomes less sensitive to γ , when compared to the hydrostatic model results. The optimal grid size parameter of $\gamma = 0.8$ can provide an accurate description of broad-band tsunami waves over varying bathymetry.

5. Numerical Experiments

The validity and interpretation of the dispersion relation (38) are illustrated through a series of numerical experiments using the hydrostatic and non-hydrostatic modes of NEOWAVE (Yamazaki et al., 2009; 2011b), which is based on the staggered finite-difference, Keller box, and semi-implicit time-integration schemes described in Section 2. NEOWAVE has been validated with the laboratory and field benchmarks by the National Tsunami Hazard Mitigation Program for hazard mapping and assessment (Yamazaki et al, 2012b; Bai et al., 2015). The use of a single computer code in this comparative study allows examination of the hydrostatic and non-hydrostatic results from the same model input and setting for the subtle difference in numerical dispersion associated with grid spacing. We first consider standing waves in a flume to examine computational errors from the implicit solution of the non-hydrostatic pressure and then illustrate effects of numerical dispersion in modeling of progressive waves on water of uniform depth.

5.1 Standing waves in a flume

The dispersion relation (38) of the non-hydrostatic model is independent of the implicit solution of the pressure Poisson equation (20). The effects of the solution scheme and its computational errors on dispersion are examined through a one-dimensional numerical experiment. Dispersion in a numerical model can be evaluated from regular standing waves of a given length in a flume of uniform depth (Bai and Cheung, 2016b). The initial static condition corresponds to a sinusoidal wave profile with a very small amplitude of $A/h = 1/4000$ to minimize nonlinear effects. Zero surface elevation is imposed at the open boundaries to restrain the node locations and thus the length of the standing waves. The period of the subsequent oscillation is defined by the dispersion property of the numerical model depending on the spatial and temporal discretizations. A numerical gauge at the center of the numerical flume records the surface elevation time series, which provides the wave period for computation of the celerity from the prescribed wavelength.

Adjustment of the water depth, time step, and grid size allows comparison of the model results with the dispersion relation (38) in terms of the parameters kh , $k\Delta x$, and Cr . Figure 5a shows the celerity as a function of $k\Delta x$ for kh up to 0.6 and a small $Cr = 0.1$. The numerical model and the dispersion relation give almost identical results at $kh = 0$, which correspond to the hydrostatic conditions. The discrepancy increases slightly with $k\Delta x$ for $kh > 0$, when the implicit solution of the non-hydrostatic pressure is involved. The computational errors, however, are very small comparing to the discretization errors in defining dispersion properties in the numerical model. Also included in the comparison is the lead-order approximation (42), which is practically identical to the dispersion relation (38) for $k\Delta x < 0.3$ independent of kh . As the accuracy is to second order, minor discrepancies develop at large values of $k\Delta x$ that are less relevant for numerical modeling. Figure 5b shows the celerity as a function of Cr while minimizing the spatial discretization errors by setting $k\Delta x = 0.1$. Because of the small values of $k\Delta x$, the celerity is not very sensitive to Cr (See Figure 2a). The good agreement between the model and analytical results over the full range of Cr reconfirms that the time step plays a secondary role in numerical dispersion.

5.2 Progressive waves in a basin

We utilize a second set of numerical experiments to illustrate manifestation of spatial discretization errors in wave propagation and anisotropy of wave dispersion over a two-dimensional Cartesian grid. The numerical experiments involve a square domain with initial conditions defined by a Gaussian hump at the center

$$\zeta(r) = Ae^{-r^2/(b/4)^2} \quad (48)$$

where r is radial distance, A is the amplitude, and b is effectively the diameter at the still-water level. The hump, which contains a range of spatial harmonics, is analogous to the static initial conditions commonly used for tsunami modeling. The resulting waves propagate radially from the center with celerity and period determined by the model dispersion property. Although the physical problem is axisymmetric, the numerical solution depends on the wave direction relative

to the principal axis. The effects of the Courant number are secondary and independent of the wave direction. We utilize a small $Cr = 0.01$ to focus on the spatial discretization, which dominates numerical dispersion. The domain has uniform water depth with grid size parameters of $\gamma = 0.8, 2$, and 4 to illustrate dispersion properties in hydrostatic and non-hydrostatic modeling from optimal to suboptimal conditions. A small wave amplitude of $A/h = 1/4000$ ensures linearity of wave propagation for evaluation and interpretation of the model results with the dispersion relation (38).

The first series of tests utilize an effective diameter of $b/h = 30$ for the Gaussian hump that the dominant harmonic is within the shallow water range. Figure 6a plots the time series and spectra at $x/h = 375$ along the axis. The non-hydrostatic solution with $\gamma = 0.8$, which closely follows the dispersion relation from Airy wave theory up to $kh = 1.2$, provides a reference for comparison. The waveform shows a distinct crest and trough profile in the form of an N -wave followed by dispersive waves with decreasing amplitude and period associated with the higher harmonics in the initial conditions. The amplitude spectrum has the peak at $kh = 0.17$ and tapers off at $kh = 0.77$. The hydrostatic solution shows a typical crest and trough profile with a larger amplitude and a longer peak period. The low numerical dispersion in the shallow-water range also leads to a more impulsive crest with the peak shewed forward. The non-hydrostatic solution continues to provide a reasonable description for the main wave component at $\gamma = 2$ albeit with a slight increase in the amplitude and period of the trailing waves. The hydrostatic solution shows reduced skewness of the leading crest as well as lagging of short-period components with increased numerical dispersion. At $\gamma = 4$, the non-hydrostatic solution overestimates dispersion with noticeable transfer of energy from the leading to the trailing waves. The hydrostatic solution closely matches the dispersion relation of Airy wave theory up to $kh = 0.6$ and produces very similar results as the non-hydrostatic solution with $\gamma = 0.8$ as shown in Figure 6b.

The second series of tests utilize an effective diameter of $b/h = 15$ for the Gaussian hump with the dominant harmonic outside the shallow-water range. Figure 7a plots the time series and spectra at $x/h = 375$. For the non-hydrostatic solution with $\gamma = 0.8$, the time series shows a wave

544 train with decreasing amplitude and period typical of a dispersive system. The spectrum has a
 545 peak at $kh = 0.44$ with energy up to $kh = 0.96$ inside the range of accurate model dispersion. The
 546 hydrostatic solution produces a distinct initial crest and trough profile followed by short-period
 547 waves. Since the initial conditions defines the spectral components spatially in terms of the
 548 wavelength, the overestimated celerity, as shown in Figure 4a, leads to underestimation of the
 549 wave period. Dispersion is instrumental in eliminating these short-period artifacts commonly
 550 seen in hydrostatic modeling of tsunamis (Bai and Cheung, 2016a; Li et al., 2016). The non-
 551 hydrostatic solution still resolves the initial wave accurately with $\gamma = 2$, but the slightly
 552 underestimated celerity with increasing kh results in overestimation of the period and amplitude
 553 for the trailing waves. The increased numerical dispersion in the hydrostatic model produces a
 554 less impulsive initial crest and longer trailing waves with improved description of amplitude
 555 attenuation. At $\gamma = 4$, the excess dispersion in the non-hydrostatic model leads to shifting of the
 556 largest peak to the second wave. The hydrostatic model resolves dispersion in the shallow-water
 557 range, and as illustrated in Figure 7b, reproduces the longer-period initial waves from the non-
 558 hydrostatic solution with $\gamma = 0.8$. The short-period trailing waves, which are outside the range of
 559 numerical dispersion, are slowly attenuating on the fringe of numerical noise.

560 The numerical results have demonstrated the lead-order dispersion relation (42), which
 561 indicates reduced influence of discretization when intrinsic dispersion is present in the model.
 562 This is evident in the subtle variation of the non-hydrostatic solution versus the transformation of
 563 the hydrostatic solution from non-dispersive to weakly dispersive over the range of γ from 0.8 to
 564 4. We utilize the test with $b/h = 15$ and $\gamma = 2$ that involves suboptimal numerical dispersion in
 565 both the hydrostatic and non-hydrostatic models, to examine manifestation of discretization
 566 errors in oblique propagation directions and the concept of effective grid spacing as suggested in
 567 the lead-order dispersion relation. Figure 8 plots the time series and spectra at $r/h = 375$ for wave
 568 directions of 0° , 22.5° , and 45° relative to the x axis. Numerical dispersion attenuates with wave
 569 obliquity in both the hydrostatic and non-hydrostatic solutions, but the effects are more
 570 significant in the former due to the absence of intrinsic dispersion, as demonstrated by the

increasing leading wave amplitude. The parameter β decreases from 1 to $3/4$ as the wave direction turns from the x axis to 22.5° and reaches the minimum at $1/2$ for propagation along the grid diagonal. The results at 22.5° and 45° corroborate those along the x axis from a separate set of tests using reduced grid size parameters of $k(\sqrt{\beta}\Delta x)$ with $\beta = 3/4$ and $1/2$. The minor discrepancies are due to interpolation of the surface elevation from adjacent grid points. The use of effective grid spacing provides an intuitive assessment of numerical dispersion in practical application.

6. Case Study

The 2011 Mw 9.1 Tohoku earthquake ruptured the megathrust off northeastern Japan with strong shaking and a destructive tsunami across the region (Hayes, 2011; Mori et al., 2011). The event produced unprecedented geophysical and hydrographic datasets for development of a range of earthquake and tsunami source models to understand the mechanisms and impacts (Lay, 2018). The tsunami and P-wave constrained model (TP-MOD) of Yamazaki et al. (2018) consistently reproduces the global seismic and regional geodetic records through a finer-scale moment and rake constrained inversion as well as wave runup along 2000 km of east Japan coasts, near-field waveforms at 18 buoys surrounding the tsunami source, and far-field waveforms from 26 DART stations across the north and south Pacific using NEOWAVE. The Pacific Ocean has an average depth of 4,000 m, while having a general range of 2000 to 6000 m associated with large-scale seafloor features such as basins and rises. Their grid size of 2 arcmin and the average depth of the Pacific give $\gamma \approx 0.8$, which produces optimal performance for wave dispersion in the open ocean. The value of γ ranges from 0.4 to 3.2 over large-scale seafloor features, but the effective grid size for oblique wave directions and the decreasing grid spacing with latitude reduce the actual value of γ and the level of undesirable numerical dispersion in the non-hydrostatic solution. The good agreement over extended durations between the computed and recorded tsunami waveforms at locations as far as the Chile coasts indicates accurate

reproduction of the seafloor deformation at the tsunami source as well as the propagation processes across 16,000 km of the ocean for a comparative study.

We utilize TP-MOD to define the seafloor deformation sequence for modeling of the 2011 Tohoku tsunami across the North Pacific using NEOWAVE. The model input and setting from Yamazaki et al. (2018) provide the basis for a grid sensitivity analysis in hydrostatic and non-hydrostatic computations of tsunami waves with varying bathymetry. Figure 9a shows the fault-slip distribution and seafloor displacement at the end of the 2.5 min rupture. The dislocation extends 240 km along dip and 400 km along strike with average slip reaching 22 and 37 m at subfaults near the epicenter and trench. Implementation of the planar fault solution of Okada (1985) provides the time history of seafloor vertical displacement, which in turn is augmented by horizontal displacement on local slopes (Tanioka and Satake, 1996), for modeling of tsunami generation via the non-hydrostatic terms in NEOWAVE. The final deformation with up to 2 m of subsidence near the coast, 9 m of uplift adjacent to the epicenter, and 7 and 33 m of vertical and horizontal displacements near the trench is consistent with the geodetic records from Iinuma et al. (2012) and Ito et al. (2011). Both the hydrostatic and non-hydrostatic modeling of the tsunami utilizes 1, 2, and 5 arcmin grid spacing to examine sensitivity of numerical dispersion across the Pacific. A two-way nested 1-arcmin grid is implemented over the source region within the 2 and 5-arcmin grids as shown in Figure 9b. For hydrostatic modeling, the vertical velocity term is disabled after the tsunami is generated and the resulting nonlinear shallow-water equations are integrated with the semi-implicit scheme for the rest of the computation. The use of the same tsunami generation mechanism and near-field resolution in the hydrostatic and non-hydrostatic computations allows direct comparison of the results to quantify dispersion effects from trans-oceanic propagation.

Figures 10 and 11 compare the non-hydrostatic and hydrostatic solutions at 6 and 8 hours after the earthquake as the tsunami passes through the western and major Hawaiian Islands. The dominant 45, 60, and 90-min components associated with the overall slip near the epicenter and trench are in the shallow-water range across the Pacific (Yamazaki et al., 2018), but effects of

dispersion or the lack of it are seen from the source to the wave front. The non-hydrostatic model with the 2-arcmin grid, which at $\gamma \approx 0.8$, has the optimal combination of intrinsic and numerical dispersion over a wide kh range (Figure 4b), provides a reference for comparison. The modeled waves show decreasing amplitude and period behind the leading crest. The many seamounts and atolls in the western and central Pacific produce prominent scattering of the trailing waves due to their shorter wavelengths associated with the detailed slip pattern. The hydrostatic model at the same resolution underestimates dispersion even in the shallow-water range (Figure 4a). This results in larger and more impulsive leading waves crisscrossed and followed by notably shorter trailing waves in contrast to the non-hydrostatic solution. Scattering of the trailing waves over seamounts generates short-period signals down to 3 min period due to the lack of dispersion and overestimation of the celerity locally. The artifacts are most evident along the Emperor Seamounts and the Hawaiian Islands obscuring the tsunami wave patterns. The hydrostatic model results from the 5-arcmin grid can reproduce dispersion around the shallow-water range with $\gamma \approx 4$ (Figure 4a). The amplitude and timing of the dominant components near the wave front compare reasonably well with the non-hydrostatic solution, but the short-period artifacts remains in the trailing wave system due to the limited range of dispersion through numerical discretization alone.

Dispersion plays a significant role in the overall amplitude of trans-oceanic tsunamis that has significant implications for hazard mapping and warning as well as engineering design. Figure 12 plots the reference wave amplitude from the 2-arcmin non-hydrostatic computation as well as the amplitude difference from those obtained using grid sizes of 1 to 5 arcmin with and without intrinsic dispersion. The reference wave amplitude shows multiple energy lobes radiating from the source off the Tohoku coast across the North Pacific. The non-hydrostatic solution at finer grid spacing of 1 arcmin involves an 8-fold increase of the computing time, but exhibits negligible differences from the reference amplitude, as intrinsic dispersion in the governing equations is sufficient to describe the propagation processes and numerical dispersion is small for the grid spacing. Increasing the grid size to 5 arcmin overshoots numerical dispersion

resulting in moderate reduction of wave amplitude primarily along the main energy lobes. Switching the non-hydrostatic terms off reduces the computing time by a factor of four in NEOWAVE. The lack of intrinsic dispersion results in overestimation of the wave amplitude across most of the North Pacific. Increasing the grid size enhances numerical dispersion with gradual reduction of the wave amplitude. The 5-arcmin grid can generate enough dispersion around the shallow-water range to account for the dominant wave components. The overestimated amplitude is due to insufficient dispersion of short-period waves as well as presence of high-frequency artifacts trailing the leading waves. The large grid size of more than two times the average water depth might not fully resolve the small islands and seamounts as most evident in the wave amplitude overestimation in the well-sheltered Sea of Okhotsk and Sea of Japan.

Tables 1 and 2 compare the computed initial peak amplitude and arrival time with observations at selected DART stations across the North Pacific (see Figure 12 for station locations). The comparison at DART 21418, which is located 550 km from the source with relatively uniform bathymetry in between, provides a straightforward demonstration of dispersion as in the Gaussian hump numerical experiment. The non-hydrostatic computations at 1 and 2-arcmin grid spacing ($\gamma \leq 0.8$) give good agreement with the observed wave amplitude through a combination of intrinsic and numerical dispersion. The computed amplitude deteriorates slightly at lower resolution due to excess numerical dispersion from the spatial discretization. The hydrostatic model produces the optimal amount of discretization errors at 5 arcmin ($\gamma \approx 4$) in matching the observation, but overestimates the amplitude at higher resolution due to insufficient dispersion. Tsunami arrival time is also influenced by earth elasticity and water density variation (Tsai et al., 2013; Baba et al., 2017), which are typically not included in the governing equations for free-surface flow. The absence of these high-order physical processes leads to early arrivals in both hydrostatic and non-hydrostatic modeling of trans-oceanic tsunamis (Bai and Cheung, 2016a). At DART 21418, the initial peak from the non-hydrostatic computation arrives 1/3 min early relatively independent of the grid spacing. The

more impulsive initial crest from the hydrostatic solution leads to an earlier arrival of the peak as seen in the Gaussian hump experiment (Figures 6 and 7). The skewness of the computed initial crest is large and is an important factor for the timing of the peak in the near field, but is somewhat reduced by numerical dispersion, when the grid spacing is increased to 5 arcmin and improved agreement of the arrival time is observed.

The physical processes become more complex in the far field and the wave pattern is influenced by additional factors such as refraction, diffraction, and reflection of the broad-band components. The effects are most pronounced at DART 21415 immediately to the east of the Emperor Seamount chain across from the tsunami source. The non-hydrostatic model continues to produce consistent results for the peak amplitude and arrival time that demonstrate convergence of the solution at 2-arcmin or finer grid spacing. The offsets from observations are due to approximation or omission of physical processes other than dispersion. The hydrostatic solution maintains the general trend associated with numerical dispersion, but shows variations depending on the model resolution and station location. The peak arrival time is closer to the non-hydrostatic prediction albeit with interference from the short-period artifacts and is less sensitive to grid spacing at the far-field locations, as wave skewness reduces with numerical dispersion over long distance of propagation. Except for DART 21415, the travel time from the non-hydrostatic and hydrostatic models is typically 1 and 2% shorter comparing to the observations. The ~1% difference between the two approaches is due to the respective celerity of the long-period leading waves. The effects of intrinsic and numerical dispersion on arrival time are secondary comparing to the peak amplitude, which is influenced by harmonic components outside the shallow-water range. The computed peak amplitude from the hydrostatic model at 1 and 2-arcmin grid spacing can be 40% larger due to phase locking, but even at the optimal resolution of 5 arcmin, does not necessarily approach the non-hydrostatic solution. In contrast to the Gaussian hump experiment, the use of numerical dispersion through adjustment of grid spacing in a hydrostatic model does not always provide reliable wave amplitude in real-world applications.

7. Discussion and Conclusions

The Fourier method is an effective and straightforward alternative to the Taylor expansion in deriving dispersion relations for high-order wave models through the eigenvalue of the discretized linear governing equations. The present study focuses on one-layer non-hydrostatic flows for tsunami modeling, but the approach can be readily applied to multi-layer or Boussinesq-type models for wind-generated waves. The extension of the Fourier method from hydrostatic to non-hydrostatic models simply increases the rank of the eigenvalue matrix from three to five. The eigenvalue gives rise to a stability condition for the numerical scheme as well as a combined relation for intrinsic dispersion from the continuous governing equations and numerical dispersion as a phase error associated with the spatial and temporal discretizations. The discretization with a staggered finite-difference grid and first-order semi-implicit time integration remains neutrally stable with inclusion of the non-hydrostatic terms through the Keller box scheme. The dispersion relation is independent of the implicit solution of the non-hydrostatic pressure and is exact for linear wave propagation over uniform depth. Implementation of Taylor expansions to the dispersion relation produces a lead-order approximation, which demonstrates the interrelationship among the depth and discretization parameters in modulating dispersion.

The exact and lead-order dispersion relations provide insights into the interplay between intrinsic and numerical dispersion during the computation as well as a useful tool to guide selection of discretization parameters for practical application. The depth parameter kh and spatial discretization $k\Delta x$ have complementary effects on dispersion providing a means to optimize non-hydrostatic wave models through adjustment of the grid size. Their coupling results in notable reduction of numerical dispersion outside the shallow-water range in comparison to the hydrostatic model. The temporal discretization tends to reduce numerical dispersion, but the effects are secondary within the range of Courant numbers used in wave modeling. Numerical dispersion, which results primarily from truncation errors associated with

the spatial discretization, decreases for oblique wave propagation due to effective increase in resolution and reaches a minimum at 45° from a principal axis of the grid. The intrinsic property from the continuous governing equations accounts for a significant portion of physical dispersion and reduces the effects of spatial discretization, thereby improving numerical modeling of broadband wave propagation.

Discretization errors in shallow-water models can mimic the lead-order dispersion term from Boussinesq-type systems for tsunami modeling, but the required grid size might not be sufficient to resolve the many seamounts and islands across the Pacific. In addition, the lead-order dispersion does not cover the full spectrum of tsunami waves, resulting in phase-locking of harmonic components during propagation and high-frequency noise across the ocean. The wave amplitude from a hydrostatic model is influenced by these numerical artifacts and sensitive to the spatial resolution commonly used in tsunami modeling. The Boussinesq-type equations, which have accurate dispersion in the tsunami range, might be adversely affected by numerical dispersion. A tsunami consists of a number of harmonics related to the complexity of the seafloor bathymetry and deformation at the source. The wave components with varying dispersion properties need to be captured by a computational grid spanning across the ocean. The Keller box scheme leads to slight underestimation of dispersion in the governing equations of the non-hydrostatic model. The numerical solution can be tuned with grid spacing to achieve good and consistent convergence properties. The use of a 2-arcmin grid is optimal in balancing intrinsic and numerical dispersion over the varying bathymetry across the Pacific Ocean.

The use of two-way nested grids with increasing resolution from the open ocean to the coast has been a standard practice in tsunami hazard mapping (e.g., Imamura et al. 1988; Liu et al. 1995; Yamazaki et al., 2011b). For example, the resolution can span a wide range from 2 arcmin (~ 3700 m near the equator) across the Pacific Ocean to as fine as ~ 5 to 10 m at the shore (e.g., Bai et al., 2018a; Yamazaki et al., 2018). The primary purpose of grid refinement is to more precisely capture shelf and coastal features, which play an important role in wave amplification and coastal inundation. Although the present study focuses on trans-oceanic tsunami propagation,

the dispersion relation can provide guidance for grid refinement across shelf breaks. The governing equations of the non-hydrostatic model can describe dispersion within the tsunami range reasonably well. The numerical means only serves as a secondary and convenient measure to improve the wave propagation property. There exists an optimal grid size to water depth ratio, but it is not necessary to keep refining the grid toward the shore, because physical dispersion vanishes in the sheet flow as the water depth parameter $kh \rightarrow 0$ and numerical dispersion is negligible within the range of $k\Delta x$ commonly used for inundation modeling.

Acknowledgments

The authors received support from the National Tsunami Hazard Mitigation Program grants NA16NWS4670036 and NA17NWS4670012 through Hawaii Emergency Management Agency. We would like to thank Yoshiki Yamazaki for the assistance with implementation of NEOWAVE in this study as well as Yefei Bai, Troy Heitmann, Pieter Smit, and the three anonymous reviewers for their helpful comments that have improved this paper. SOEST Contribution No. 10637.

Appendix A

We use the Taylor method to analyze the semi-implicit time integration used in NEOWAVE of Yamazaki et al. (2009, 2011b) for a direct comparison with the truncation properties in the leap-frog scheme. Considering one-dimensional linear wave propagation with uniform depth, the discretized governing equations for the hydrostatic component are written as:

$$\frac{U_{i+1/2}^{m+1} - U_{i+1/2}^m}{\Delta t} + g \frac{\zeta_{i+1}^m - \zeta_i^m}{\Delta x} = 0 \quad (\text{A.1})$$

$$\frac{\zeta_i^{m+1} - \zeta_i^m}{\Delta t} + h \frac{U_{i+1/2}^{m+1} - U_{i-1/2}^{m+1}}{\Delta x} = 0 \quad (\text{A.2})$$

where m denotes the current time step and i is an index at the cell center. The staggered finite-difference scheme introduces second-order spatial discretization errors in the flow velocity and

surface elevation. The first-order time integration is explicit for the flow velocity in the momentum equation (A.1) and implicit for the surface elevation due to evaluation of the velocity at $(m+1)$ in the continuity equation (A.2). Applying Taylor series expansions for the variables about time step m and location i , we have

$$U_{i+1/2}^m = U_i^m + \frac{\partial U}{\partial x} \left(\frac{1}{2} \Delta x \right) + \frac{1}{2} \frac{\partial^2 U}{\partial x^2} \left(\frac{1}{2} \Delta x \right)^2 + \frac{1}{6} \frac{\partial^3 U}{\partial x^3} \left(\frac{1}{2} \Delta x \right)^3 + O(\Delta x^4) \quad (\text{A.3})$$

$$\begin{aligned} U_{i-1/2}^{m+1} = & U_i^m + \frac{\partial U}{\partial x} \left(-\frac{1}{2} \Delta x \right) + \frac{\partial U}{\partial t} (\Delta t) + \frac{1}{2} \left[\frac{\partial^2 U}{\partial x^2} \left(-\frac{1}{2} \Delta x \right)^2 + 2 \frac{\partial^2 U}{\partial x \partial t} \left(-\frac{1}{2} \Delta x \right) (\Delta t) + \frac{\partial^2 U}{\partial t^2} (\Delta t)^2 \right] \\ & + \frac{1}{6} \left[\frac{\partial^3 U}{\partial x^3} \left(-\frac{1}{2} \Delta x \right)^3 + 3 \frac{\partial^3 U}{\partial x^2 \partial t} \left(-\frac{1}{2} \Delta x \right)^2 (\Delta t) + 3 \frac{\partial^3 U}{\partial x \partial t^2} \left(-\frac{1}{2} \Delta x \right) (\Delta t)^2 + \frac{\partial^3 U}{\partial t^3} (\Delta t)^3 \right] \\ & + O(\Delta x^4, \Delta x^3 \Delta t, \Delta x^2 \Delta t^2, \Delta x \Delta t^3, \Delta t^4) \end{aligned} \quad (\text{A.4})$$

$$\begin{aligned} U_{i+1/2}^{m+1} = & U_i^m + \frac{\partial U}{\partial x} \left(\frac{1}{2} \Delta x \right) + \frac{\partial U}{\partial t} (\Delta t) + \frac{1}{2} \left[\frac{\partial^2 U}{\partial x^2} \left(\frac{1}{2} \Delta x \right)^2 + 2 \frac{\partial^2 U}{\partial x \partial t} \left(\frac{1}{2} \Delta x \right) (\Delta t) + \frac{\partial^2 U}{\partial t^2} (\Delta t)^2 \right] \\ & + \frac{1}{6} \left[\frac{\partial^3 U}{\partial x^3} \left(\frac{1}{2} \Delta x \right)^3 + 3 \frac{\partial^3 U}{\partial x^2 \partial t} \left(\frac{1}{2} \Delta x \right)^2 (\Delta t) + 3 \frac{\partial^3 U}{\partial x \partial t^2} \left(\frac{1}{2} \Delta x \right) (\Delta t)^2 + \frac{\partial^3 U}{\partial t^3} (\Delta t)^3 \right] \\ & + O(\Delta x^4, \Delta x^3 \Delta t, \Delta x^2 \Delta t^2, \Delta x \Delta t^3, \Delta t^4) \end{aligned} \quad (\text{A.5})$$

$$\zeta_{i+1}^m = \zeta_i^m + \frac{\partial \zeta}{\partial x} (\Delta x) + \frac{1}{2} \frac{\partial^2 \zeta}{\partial x^2} (\Delta x)^2 + \frac{1}{6} \frac{\partial^3 \zeta}{\partial x^3} (\Delta x)^3 + O(\Delta x^4) \quad (\text{A.6})$$

$$\zeta_i^{m+1} = \zeta_i^m + \frac{\partial \zeta}{\partial t} (\Delta t) + \frac{1}{2} \frac{\partial^2 \zeta}{\partial t^2} (\Delta t)^2 + \frac{1}{6} \frac{\partial^3 \zeta}{\partial t^3} (\Delta t)^3 + O(\Delta t^4) \quad (\text{A.7})$$

The expansions include third-order terms that are needed for analysis of discretization errors up to second order.

The Taylor method provides a step-by-step account of the truncation errors from each variable through the discretization scheme. Substitution of the expanded variables from equations (A.2) to (A.7) into the momentum equation (A.1) and the continuity equation (A.2) gives

$$\begin{aligned} \frac{\partial U}{\partial t} + g \frac{\partial \zeta}{\partial x} + \frac{\Delta x}{2} \left(\frac{\partial^2 U}{\partial x \partial t} + g \frac{\partial^2 \zeta}{\partial x^2} \right) + \frac{\Delta t}{2} \frac{\partial^2 U}{\partial t^2} + \frac{(\Delta x)^2}{24} \left(3 \frac{\partial^3 U}{\partial x^2 \partial t} + 4g \frac{\partial^3 \zeta}{\partial x^3} \right) \\ + \frac{(\Delta t)^2}{6} \frac{\partial^3 U}{\partial t^3} + \frac{(\Delta x)(\Delta t)}{4} \frac{\partial^3 U}{\partial x \partial t^2} = O(\Delta x^3, \Delta x^2 \Delta t, \Delta x \Delta t^2, \Delta t^3) \end{aligned} \quad (\text{A.8})$$

$$\begin{aligned} \frac{\partial \zeta}{\partial t} + h \frac{\partial U}{\partial x} + \Delta t \left(\frac{1}{2} \frac{\partial^2 \zeta}{\partial t^2} + h \frac{\partial^2 U}{\partial x \partial t} \right) + \frac{(\Delta x)^2}{24} \left(h \frac{\partial^3 U}{\partial x^3} \right) + \frac{(\Delta t)^2}{6} \left(\frac{\partial^3 \zeta}{\partial t^3} + 3h \frac{\partial^3 U}{\partial x \partial t^2} \right) \\ = O(\Delta x^2 \Delta t, \Delta t^3) \end{aligned} \quad (\text{A.9})$$

which can be rewritten as

$$\frac{\partial U}{\partial t} = -g \frac{\partial \zeta}{\partial x} + O(\Delta x, \Delta t) \quad (\text{A.10})$$

$$\frac{\partial \zeta}{\partial t} = -h \frac{\partial U}{\partial x} + O(\Delta x^2, \Delta t) \quad (\text{A.11})$$

Their higher-order time derivatives can be expressed in terms of spatial derivatives as

$$\frac{\partial^2 U}{\partial t^2} = -g \frac{\partial^2 \zeta}{\partial x \partial t} + O(\Delta x, \Delta t) = g \frac{\partial^2 U}{\partial x^2} + O(\Delta x, \Delta t) \quad (\text{A.12})$$

$$\frac{\partial^2 \zeta}{\partial t^2} = -h \frac{\partial^2 U}{\partial x \partial t} + O(\Delta x^2, \Delta t) = gh \frac{\partial^2 \zeta}{\partial x^2} + O(\Delta x, \Delta t) \quad (\text{A.13})$$

$$\frac{\partial^3 U}{\partial t^3} = -g \frac{\partial^3 \zeta}{\partial x \partial t^2} + O(\Delta x, \Delta t) = -g^2 h \frac{\partial^3 \zeta}{\partial x^3} + O(\Delta x, \Delta t) \quad (\text{A.14})$$

$$\frac{\partial^3 \zeta}{\partial t^3} = gh \frac{\partial^3 \zeta}{\partial x^2 \partial t} + O(\Delta x, \Delta t) = -gh^2 \frac{\partial^3 U}{\partial x^3} + O(\Delta x, \Delta t) \quad (\text{A.15})$$

Substitution of the high-order time derivatives into the momentum and continuity equations (A.8)

and (A.9) gives

$$\frac{\partial U}{\partial t} + g \frac{\partial \zeta}{\partial x} + \frac{\Delta t}{2} \frac{\partial^2 U}{\partial t^2} + \frac{(\Delta x)^2}{24} \left(g \frac{\partial^3 \zeta}{\partial x^3} \right) - \frac{(\Delta t)^2}{6} \left(g^2 h \frac{\partial^3 \zeta}{\partial x^3} \right) = O(\Delta x^3, \Delta x^2 \Delta t, \Delta x \Delta t^2, \Delta t^3) \quad (\text{A.16})$$

$$\frac{\partial \zeta}{\partial t} + h \frac{\partial U}{\partial x} + \frac{\Delta t}{2} \left(h \frac{\partial^2 U}{\partial x \partial t} \right) + \frac{(\Delta x)^2}{24} \left(h \frac{\partial^3 U}{\partial x^3} \right) + \frac{(\Delta t)^2}{12} \left(gh^2 \frac{\partial^3 U}{\partial x^3} \right) = O(\Delta x^2 \Delta t, \Delta t^2 \Delta x, \Delta t^3) \quad (\text{A.17})$$

each of which contains a first-order error term introduced by the time integration. The use of the

velocity at $(m+1)$ in the integration of the surface elevation produces the cross derivative in

equation (A.17) that cancels the first-order error term in equation (A.16) upon combination of the two. The resulting wave equation reads

$$\frac{\partial^2 \zeta}{\partial t^2} - gh \frac{\partial^2 \zeta}{\partial x^2} - gh \left[\frac{(\Delta x)^2}{12} - \frac{(\Delta t)^2}{12} gh \right] \frac{\partial^4 \zeta}{\partial x^4} = O(\Delta x^3, \Delta x^2 \Delta t, \Delta x \Delta t^2, \Delta t^3) \quad (\text{A.18})$$

which is identical to that derived from the leap-frog scheme by Imamura et al. (1988). The discretization introduces numerical dispersion in an otherwise hyperbolic system through the fourth-order spatial derivative of the surface elevation. The coefficient $(\Delta x)^2/12$ of the dispersion term reflects the second-order spatial discretization with the staggered finite-difference grid, while $(\Delta t)^2/12$ infers second-order truncation properties in the semi-implicit time integration.

References

- Abbott M. B., McCowan A. D., Warren I. R., 1984. Accuracy of short-wave numerical models. *J. Hydraulic Eng.* 110(10), 1287–1301. doi:10.1061/(ASCE)0733-9429(1984)110:10(1287).
- Baba, T., Allgeyer, S., Hossen, J., Cummins, P.R., Tsushima, H., Imai, K., Yamashita, K., Kato, T., 2017. Accurate numerical simulation of the far-field tsunami caused by the 2011 Tohoku earthquake, including the effects of Boussinesq dispersion, seawater density stratification, elastic loading, and gravitational potential change. *Ocean Modell.* 111, 46-54.
- Bai, Y., Cheung, K.F., 2013. Dispersion and nonlinearity of multi-layer non-hydrostatic free-surface flow. *J. Fluid Mech.* 726, 226-260.
- Bai, Y., Cheung, K.F., 2016a. Hydrostatic versus non-hydrostatic modeling of tsunamis with implications for insular shelf and reef environments. *Coast. Eng.* 117, 32-43.
- Bai, Y., Cheung, K.F., 2016b. Linear and nonlinear properties of reduced two-layer models for non-hydrostatic free-surface flow. *Ocean Modell.* 107, 64–81. doi: 10.1016/j.ocemod.2016.10.003.
- Bai, Y., Yamazaki, Y., Cheung, K.F., 2018a. Amplification of drawdown and runup over Hawaii's insular shelves by tsunami N-waves from mega Aleutian earthquakes. *Ocean Modell.* 124, 61-74.
- Bai, Y., Ye, L., Yamazaki, Y., Lay, T., and Cheung, K.F. 2018b. The 4 May 2018 Mw 6.9 Hawaii Island earthquake and implications for tsunami hazards. *Geophys. Res. Lett.* 45(20), 11,040-11,049.
- Bai Y., Yamazaki Y., Cheung, K. F., 2018c. Convergence of multilayer nonhydrostatic models in relation to Boussinesq-type equations. *J. Waterw. Port Coast. Ocean Eng.* 144(2), 06018001. doi: 10.1061/(ASCE)WW.1943-5460.0000438.

842 Bai, Y., Yamazaki, Y., and Cheung, K.F. 2015. NEOWAVE. Proceedings and Results of the
 843 2015 National Tsunami Hazard Mitigation Program Model Benchmarking Workshop,
 844 Portland, Oregon, 165-177.
 845 Bricker, J. D., Munger, S., Pequignet, C., Wells, J. R., Pawlak, G., Cheung, K. F., 2007. ADCP
 846 observations of edge waves off Oahu in the wake of the November 2006 Kuril Islands
 847 tsunami. *Geophys. Res. Lett.* 34(23). doi:10.1029/2007GL032015.
 848 Burwell, D., Tolkova E., Chawla A., 2007. Diffusion and dispersion characterization of a
 849 numerical tsunami model. *Ocean Modell.* 19(1), 10–30. doi:10.1016/j.ocemod.2007.05.003.
 850 Cheung, K.F., Bai, Y., Yamazaki, Y., 2013. Surges around the Hawaiian Islands from the 2011
 851 Tohoku tsunami. *J. Geophys. Res. Oceans* 118(10), 5703-5719, doi: 10.1002/jgrc.20413.
 852 Cho, Y.-S., 1995, Numerical simulations of tsunami propagation and run-up, Ph.D. thesis.
 853 Cornell University, Ithaca, New York.
 854 Cho, Y.-S., Sohn D.-H., Lee S. O., 2007. Practical modified scheme of linear shallow-water
 855 equations for distant propagation of tsunamis, *Ocean Eng.* 34(11), 1769–1777.
 856 doi: 10.1016/j.oceaneng.2006.08.014.
 857 Chorin, A., 1968. Numerical solution of the Navier-Stokes equations. *Math. Comput.* 22(104),
 858 745-762.
 859 Foreman, M. G. G., 1984. A two-dimensional dispersion analysis of selected methods for solving
 860 the linearized shallow water equations. *J. Comput. Phys.* 56(2), 287–323. doi: 10.1016/0021-
 861 9991(84)90097-4.
 862 Gobbi, M. F., Kirby J. T., Wei GE, 2000. A fully nonlinear Boussinesq model for surface waves.
 863 Part 2. Extension to $O(kh)^4$, *J. Fluid Mech.* 405, 181–210. doi: 10.1017/S0022112099007247.
 864 Ha, T., Cho Y.-S., 2015. Tsunami propagation over varying water depths, *Ocean Eng.* 101, 67–
 865 77. doi: 10.1016/j.oceaneng.2015.04.006.
 866 Hanson, J. A., Bowman J. R., 2005. Dispersive and reflected tsunami signals from the 2004
 867 Indian Ocean tsunami observed on hydrophones and seismic stations. *Geophys. Res. Lett.*
 868 32(17). doi: 10.1029/2005GL023783.
 869 Hayes, G.P., 2011. Rapid source characterization of the 2011 Mw 9.0 off the Pacific coast of
 870 Tohoku earthquake. *Earth Planets Space* 63(7), 529-534.
 871 <https://doi.org/10.5047/eps.2011.05.012>.
 872 Horrillo, J., Kowalik, Z., Shigihara Y., 2006. Wave dispersion study in the Indian Ocean-
 873 Tsunami of December 26, 2004. *Mar. Geod.* 29(3), 149–166. doi:
 874 10.1080/01490410600939140.
 875 Imamura, F., Shuto N., Goto C., 1988. Numerical simulations of the transoceanic propagation of
 876 tsunamis, in Sixth Congress of the Asian and Pacific Regional Division, Int. Assoc. Hydraul.
 877 Res., Kyoto, Japan.
 878 Jeschke, A., Pedersen, G.K., Vater, S, and Behrens, J., 2017. Depth-averaged non-hydrostatic
 879 extension for shallow-water equations with quadratic vertical pressure profile: Equivalence to
 880 Boussinesq-type equations. *Int. J. Numer. Meth. Fluids* 84(10), 569-583.
 881 Iinuma, T., Hino, R., Kido, M., Inazu, D., Osada, Y., Ito, Y., Ohzono, M., Tsushima, H., Suzuki,
 882 S., Fujimoto, H., and Miura, S., 2012. Coseismic slip distribution of the 2011 off the Pacific

coast of Tohoku Earthquake inferred from seafloor geodetic data. *J. Geophys. Res.* 117, B07409, doi:10.1029/2012JB009186

Ito, T., Ozawa, K., Watanabe, T., and Sagiya, T., 2011. Slip distribution of the 2011 off the Pacific coast of Tohoku Earthquake inferred from geodetic data. *Earth Planets Space*, 63(7), 627-630, doi:10.5047/eps.2011.06.023.

Kirby, J. T., Shi F., Tehranirad B., Harris J. C., Grilli S. T., 2013. Dispersive tsunami waves in the ocean: Model equations and sensitivity to dispersion and Coriolis effects. *Ocean Modell.* 62, 39–55. doi: 10.1016/j.ocemod.2012.11.009.

Kowalik, Z., Bang I., 1987. Numerical computation of tsunami run-up by the upstream derivative method. *Sci. Tsunami Haz.* 5(2), 77–84.

Kowalik, Z., Murty, T.S., 1993. *Numerical Modeling of Ocean Dynamics*. World Scientific, Singapore.

Kulikov, E., 2006. Dispersion of the Sumatra tsunami waves in the Indian Ocean detected by satellite altimetry. *Russ. J. Earth Sci.* 8. doi: 10.2205/2006ES000214.

Lay, T., 2018. A review of the rupture characteristics of the 2011 Tohoku-oki Mw 9.1 earthquake. *Tectonophysics* 733, 4-36.

Lay, T., Ye, L., Kanamori, H., Yamazaki, Y., Cheung, K.F., Kwong, K., and Koper, K.D., 2013. The October 28, 2012 Mw 7.8 Haida Gwaii underthrusting earthquake and tsunami: Slip partitioning along the Queen Charlotte Fault transpressional plate boundary. *Earth Planet. Sci. Lett.* 375, 57-70.

Leendertse, J. J., 1967. Aspects of a computational model for long-period water-wave propagation. Report RM-5294-PR, The Rand Corp., Santa Monica, California.

Li, L., Cheung, K. F., Yue, H., Lay, T., Bai, Y., 2016a. Effects of dispersion in tsunami Green's functions and implications for joint inversion with seismic and geodetic data: A case study of the 2010 Mentawai Mw 7.8 earthquake. *Geophys. Res. Lett.* 43(21), 11,182–11,191. doi: 10.1002/2016GL070970.

Li, L., Lay, T., Cheung, K.F., Ye, L., 2016b. Joint modeling of teleseismic and tsunami wave observations to constrain the 16 September 2015 Illapel, Chile, Mw 8.3 earthquake rupture process. *Geophys. Res. Lett.* 43(9), 4303-4312.

Liu, P. L.-F., Cho Y.-S., Briggs M. J., Kanoglu U., Synolakis C. E., 1995. Runup of solitary waves on a circular island. *J. Fluid Mech.* 302, 259–285. doi: 10.1017/S0022112095004095.

Madsen, P. A., Murray R., Sørensen O. R., 1991. A new form of the Boussinesq equations with improved linear dispersion characteristics. *Coastal Eng.* 15(4), 371–388. doi: 10.1016/0378-3839(91)90017-B.

Mori, N., Takahashi, T., Yasuda, T., Yanagisawa, H., 2011. Survey of the 2011 Tohoku earthquake tsunami inundation and runup. *Geophys. Res. Lett.* 38(7), L00G14. <https://doi.org/10.1029/2011GL049210>.

Nwogu, O., 1993. Alternative form of Boussinesq equations for nearshore wave propagation. *J. Waterw. Port Coast. Ocean Eng.* 119(6), 618–638. doi: 10.1061/(ASCE)0733-950X(1993)119:6(618).

923 Okada, Y., 1985. Surface deformation due to shear and tensile faults in a half-space. *Bull.*
924 *Seismol. Soc. Am.* 75(4), 1135–1154.

925 Peregrine, D. H., 1967. Long waves on a beach. *J. fluid mech.* 27(4), 815–827. doi:
926 10.1017/S0022112067002605.

927 Saito, T., Matsuzawa T., Obara K., Baba T., 2010. Dispersive tsunami of the 2010 Chile
928 earthquake recorded by the high-sampling-rate ocean-bottom pressure gauges. *Geophys. Res.*
929 *Lett.* 37(23). doi: 10.1029/2010GL045290.

930 Saito, T., Inazu D., Miyoshi T., Hino R., 2014. Dispersion and nonlinear effects in the 2011
931 Tohoku-Oki earthquake tsunami. *J. Geophys. Res. Oceans* 119(8), 5160–5180. doi:
932 10.1002/2014JC009971

933 Sankaranarayanan, S., Spaulding M. L., 2003. Dispersion and stability analyses of the linearized
934 two-dimensional shallow water equations in boundary-fitted co-ordinates. *Int. J. Numer.*
935 *Meth. Fluids* 42(7), 741–763. doi: 10.1002/fld.552.

936 Shuto, N., 1991. Numerical simulation of tsunamis — Its present and near future. *Nat. Hazards*
937 4(2–3), 171–191. doi: 10.1007/BF00162786.

938 Stelling, G., Zijlema M., 2003. An accurate and efficient finite-difference algorithm for non-
939 hydrostatic free-surface flow with application to wave propagation. *Int. J. Numer. Meth.*
940 *Fluids* 43(1), 1–23. doi: 10.1002/fld.595.

941 Smit, P., Janssen, T., Holthuijsen L., Smith, J., 2014. Non-hydrostatic modeling of surf zone
942 wave dynamics. *Coastal Eng.* 83, 36–48. doi: 10.1016/j.coastaleng.2013.09.005.

943 Tanioka, Y. and Satake, K., 1996. Tsunami generation by horizontal displacement of ocean bottom.
944 *Geophys. Res. Lett.* 23(8), 861–864.

945 Titov, V. V., Synolakis C. E., 1998. Numerical modeling of tidal wave runup. *J. Waterw. Port*
946 *Coast. Ocean Eng.* 124(4), 157–171. doi: 10.1061/(ASCE)0733-950X(1998)124:4(157).

947 Tsai, V.C., Ampuero, J.P., Kanamori, H., Stevenson, D.J., 2013. Estimating the effect of earth
948 elasticity and variable water density on tsunami speeds. *Geophys. Res. Lett.* 40, 492–496.
949 <https://doi.org/10.1002/grl.50147>.

950 Vitousek, S., Fringer O. B., 2011. Physical vs. numerical dispersion in nonhydrostatic ocean
951 modeling. *Ocean Modell.* 40(1), 72–86. doi: 10.1016/j.ocemod.2011.07.002.

952 Wang, X., Liu P. L.-F., 2011. An explicit finite difference model for simulating weakly nonlinear
953 and weakly dispersive waves over slowly varying water depth. *Coastal Eng.* 58(2), 173–183.
954 doi: 10.1016/j.coastaleng.2010.09.008.

955 Warming, R. F., Hyett B. J., 1974. The modified equation approach to the stability and accuracy
956 analysis of finite-difference methods. *J. Comput. Phys.* 14(2), 159–179. doi: 10.1016/0021-
957 9991(74)90011-4.

958 Wei, G., Kirby J. T., 1995. Time-dependent numerical code for extended Boussinesq equations. *J.*
959 *Waterw. Port Coast. Ocean Eng.* 121(5), 251–261. doi: 10.1061/(ASCE)0733-
960 950X(1995)121:5(251).

961 Yamazaki, Y., Kowalik Z., Cheung K. F., 2009. Depth-integrated, non-hydrostatic model for
962 wave breaking and run-up. *Int. J. Numer. Meth. Fluids* 61(5), 473–497. doi: 10.1002/fld.1952.

- Yamazaki, Y., Lay, T., Cheung, K. F., Yue, H., Kanamori, H., 2011a. Modeling near-field tsunami observations to improve finite-fault slip models for the 11 March 2011 Tohoku earthquake. *Geophys. Res. Lett.* 38(7). doi: 10.1029/2011GL049130.
- Yamazaki, Y., Cheung K. F., Kowalik Z., 2011b. Depth-integrated, non-hydrostatic model with grid nesting for tsunami generation, propagation, and run-up. *Int. J. Numer. Meth. Fluids* 67(12), 2081–2107. doi: 10.1002/fld.2485.
- Yamazaki Y., Cheung K. F., Pawlak G., Lay T., 2012a. Surges along the Honolulu coast from the 2011 Tohoku tsunami. *Geophys. Res. Lett.* 39(9). doi: 10.1029/2012GL051624.
- Yamazaki, Y., Cheung, K.F., Kowalik, Z., Pawlak, G., and Lay, T. 2012b. NEOWAVE. Proceedings and Results of the 2011 National Tsunami Hazard Mitigation Program Model Benchmarking Workshop, Galveston, Texas, 239-302.
- Yamazaki, Y., Cheung, K. F., Lay, T., 2018. A Self-consistent Fault Slip Model for the 2011 Tohoku Earthquake and Tsunami. *J. Geophys. Res. Solid Earth* 123(2), 1435–1458. doi: 10.1002/2017JB014749.
- Yoon, S. B., 2002. Propagation of distant tsunamis over slowly varying topography. *J. Geophys. Res. Oceans* 107(C10). doi: 10.1029/2001JC000791.
- Zijlema, M., Stelling, G., Smit, P., 2011. SWASH: An operational public domain code for simulating wave fields and rapidly varied flows in coastal waters. *Coastal Eng.* 58(10), 992–1012. doi: 10.1016/j.coastaleng.2011.05.015.

List of Figures

1. Schematic of staggered finite-difference scheme for the non-hydrostatic model and illustration of effective grid spacing for wave propagation at 45° from the x axis.
2. Celerity of the non-hydrostatic model normalized by shallow-water theory as a function of $k\Delta x$ and Cr . (a) Wave propagation along the x axis. (b) Propagation at 45° from the x axis.
3. Celerity normalized by Airy wave theory as a function of $k\Delta x$ and Cr for propagation along the x axis. (a) Hydrostatic model. (b) Non-hydrostatic model. Black line denotes $c/c_{Airy} = 1$.
4. Celerity normalized by Airy wave theory as a function of kh and γ . (a) Hydrostatic model. (b) Non-hydrostatic model. Solid and dash lines indicate celerity from the dispersion relation (38) and the Boussinesq-type equations of Peregrine (1967).
5. Celerity normalized by shallow-water theory as a function of discretization parameters. (a) Grid size parameter $k\Delta x$. (b) Courant number Cr . Solid lines, dash lines, and dots denote celerity from the dispersion relation (38), the lead-order approximation (42), and numerical experiments.
6. Time series and spectra at $x/h = 375$ along the axis resulting from a Gaussian hump with an effective diameter of $b/h = 30$ at the center of the computational grid. (a) Effects of the combined grid size and depth parameter γ . (b) Comparison of the hydrostatic and non-hydrostatic solutions with $\gamma = 4$ and 0.8 respectively. Black and red lines denote hydrostatic and non-hydrostatic solutions.
7. Time series and spectra at $x/h = 375$ along the axis resulting from a Gaussian hump with an effective diameter of $b/h = 15$ at the center of the computational grid. (a) Effects of the combined grid size and depth parameter γ . (b) Comparison of the hydrostatic and non-hydrostatic solutions with $\gamma = 4$ and 0.8 respectively. Black and red lines denote hydrostatic and non-hydrostatic solutions.
8. Time series and spectra at $r/h = 375$ from a Gaussian hump with an effective diameter of $b/h = 15$ at the center of the computational grid. Black and red lines indicate hydrostatic and non-hydrostatic solutions at 0° , 22.5° , and 45° oblique angles for $\gamma = 2$. Black and red dots

denote hydrostatic and non-hydrostatic solutions obtained at the x axis using the effective grid spacing $\sqrt{\beta}\Delta x$ in separate numerical experiments.

9. Tsunami source model and computational grids. (a) Finite fault model and land surface displacement of the 2011 Tohoku earthquake from Yamazaki et al. (2018). (b) Computational domain and location map. Red star indicates the epicenter location and black rectangle delineates the nested grid when applicable.

10. Surface elevations from non-hydrostatic and hydrostatic modeling of the 2011 Tohoku tsunami at prescribed grid sizes and 6 hours after the earthquake.

11. Surface elevations from non-hydrostatic and hydrostatic modeling of the 2011 Tohoku tsunami at prescribed grid sizes and 8 hours after the earthquake.

12. Reference wave amplitude based on the 2-acrmin non-hydrostatic solution (middle panel of left column) and its difference from non-hydrostatic (top and bottom panels of left column) and hydrostatic solutions (right column) at specified grid sizes. The continuous color palette denotes the reference wave amplitude. Red and blue in the two-tone color scheme indicate overestimation and underestimation of the reference wave amplitude. Open circles and labels in the top left panel indicate DART stations.

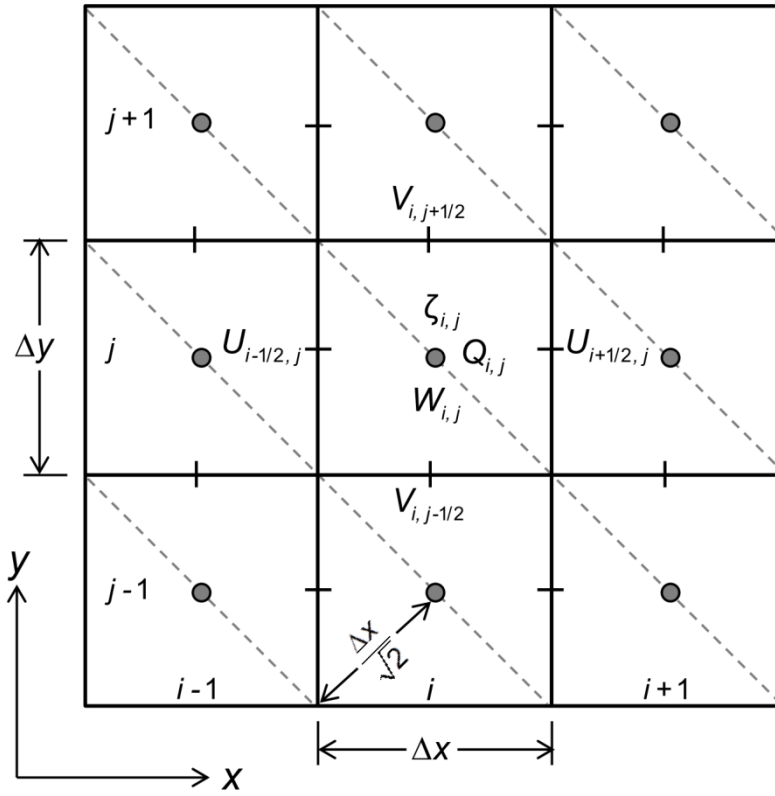


Figure 1. Schematic of staggered finite-difference scheme for the non-hydrostatic model and illustration of effective grid spacing for wave propagation at 45° from the x axis.

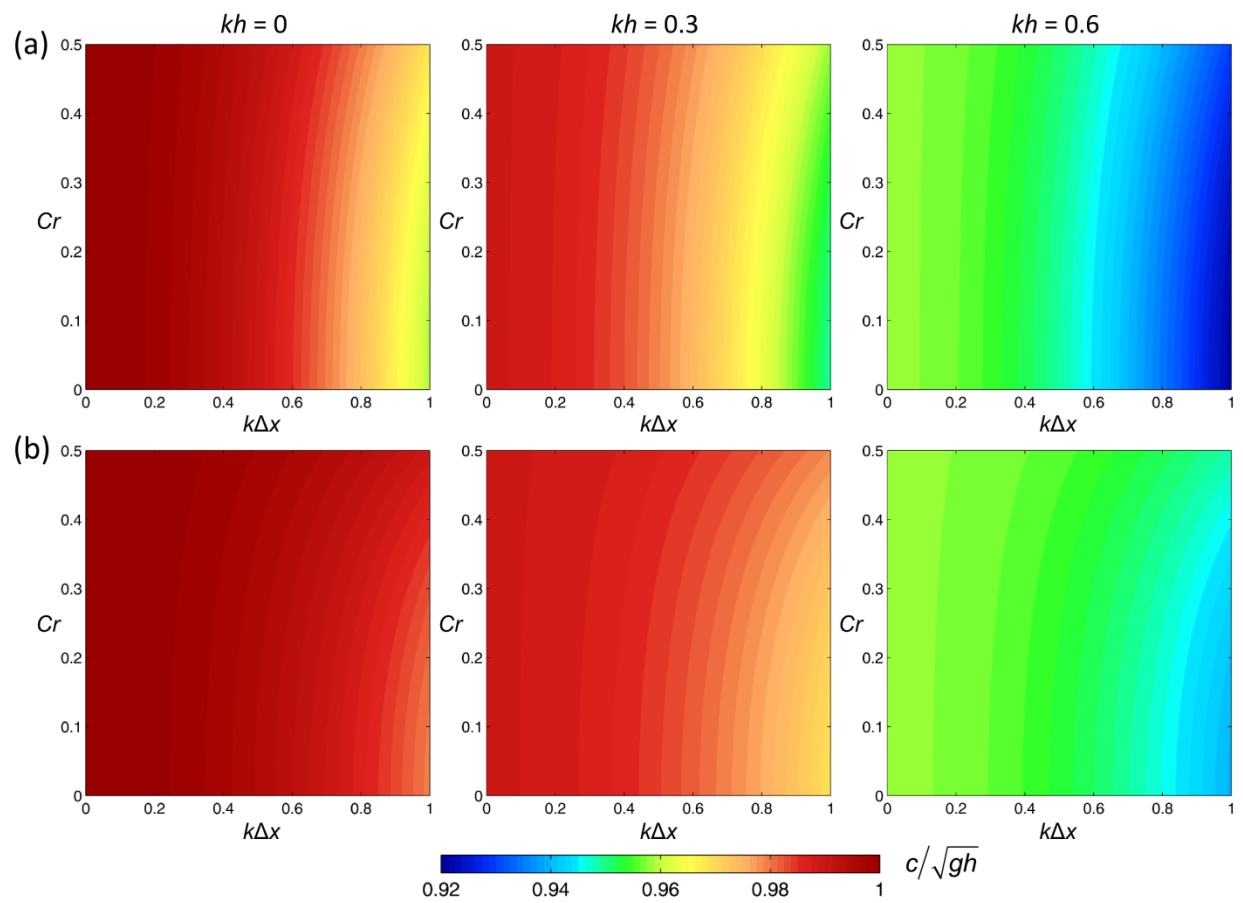
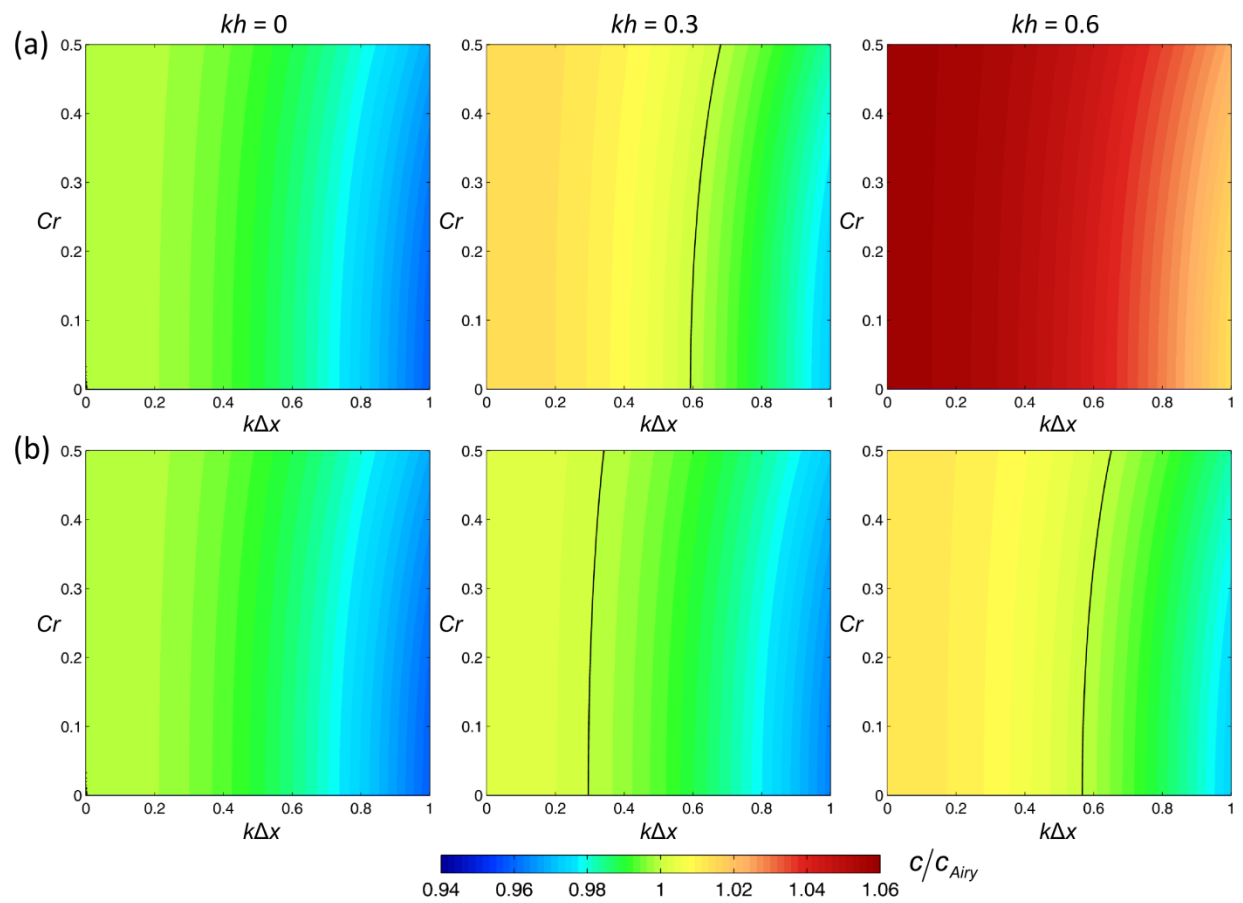


Figure 2. Celerity of the non-hydrostatic model normalized by shallow-water theory as a function of $k\Delta x$ and Cr . (a) Wave propagation along the x axis. (b) Propagation at 45° from the x axis.

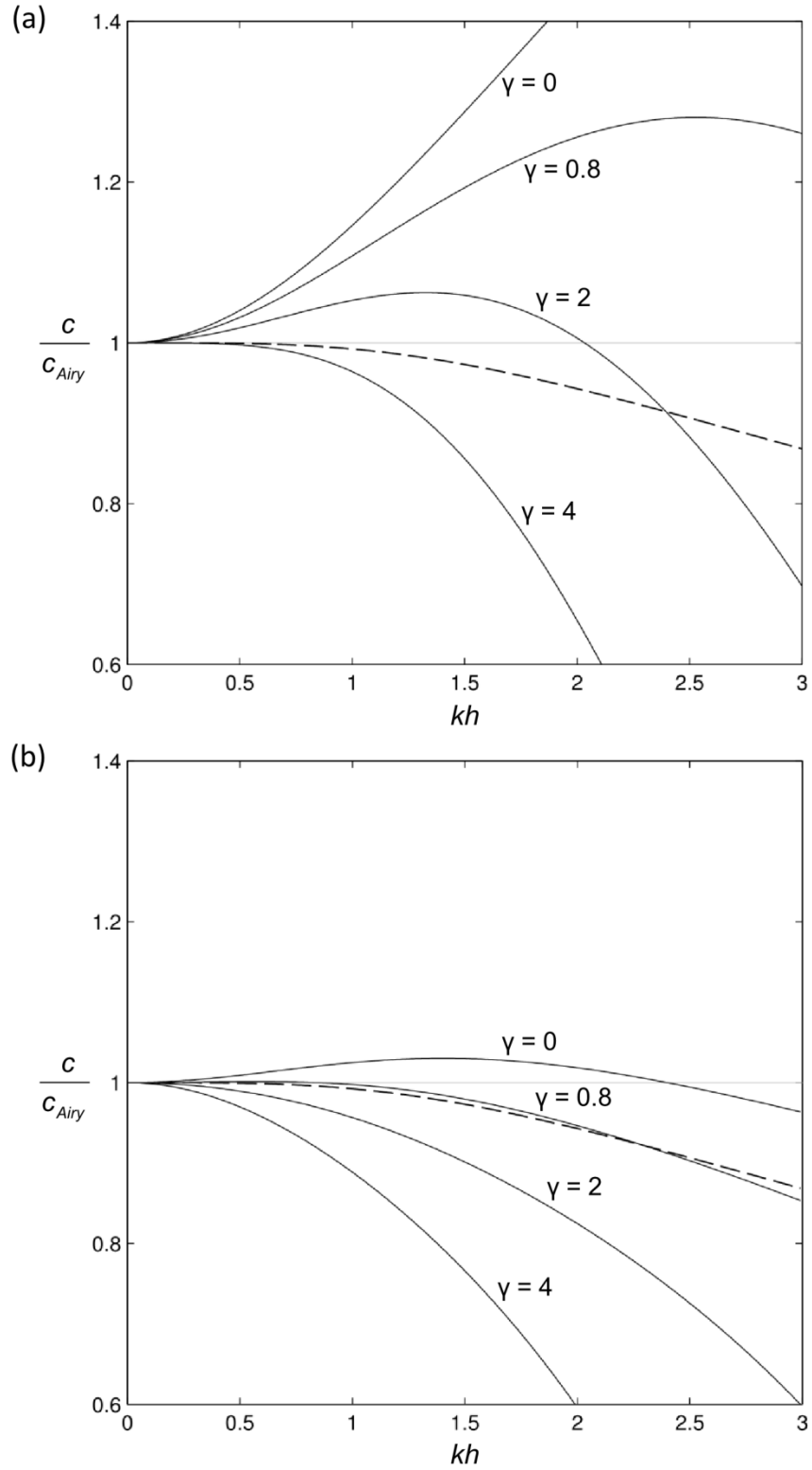


1033

1034

1035

Figure 3. Celerity normalized by Airy wave theory as a function of $k\Delta x$ and Cr for propagation along the x axis. (a) Hydrostatic model. (b) Non-hydrostatic model. Black line denotes $c/c_{Airy} = 1$.



1036

1037 Figure 4. Celerity normalized by Airy wave theory as a function of kh and γ . (a) Hydrostatic
 1038 model. (b) Non-hydrostatic model. Solid and dash lines indicate celerity from the dispersion
 1039 relation (38) and the Boussinesq-type equations of Peregrine (1967).

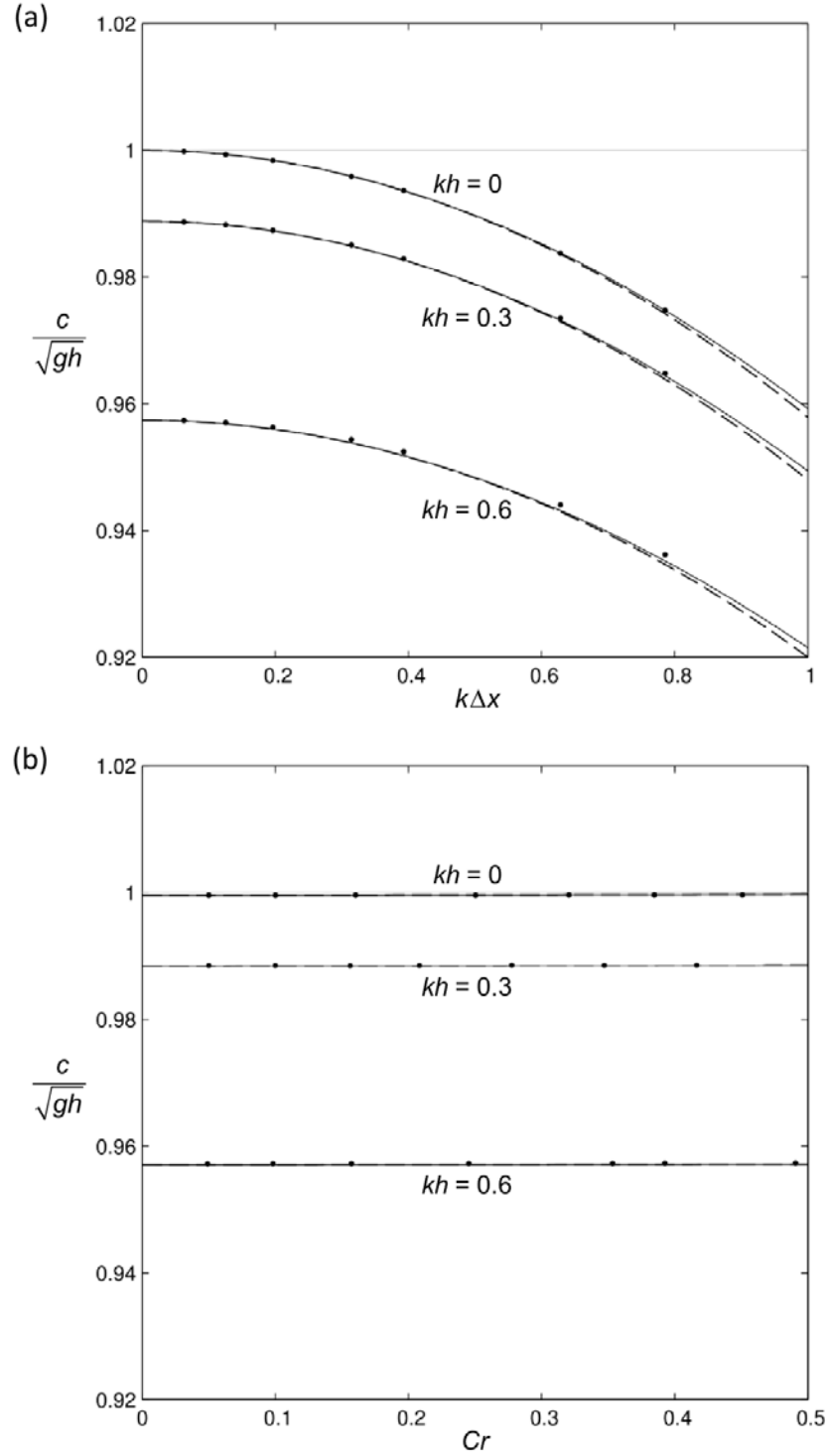


Figure 5. Celerity normalized by shallow-water theory as a function of discretization parameters. (a) Grid size parameter $k\Delta x$. (b) Courant number Cr . Solid lines, dash lines, and dots denote celerity from the dispersion relation (38), the lead-order approximation (42), and numerical experiments.

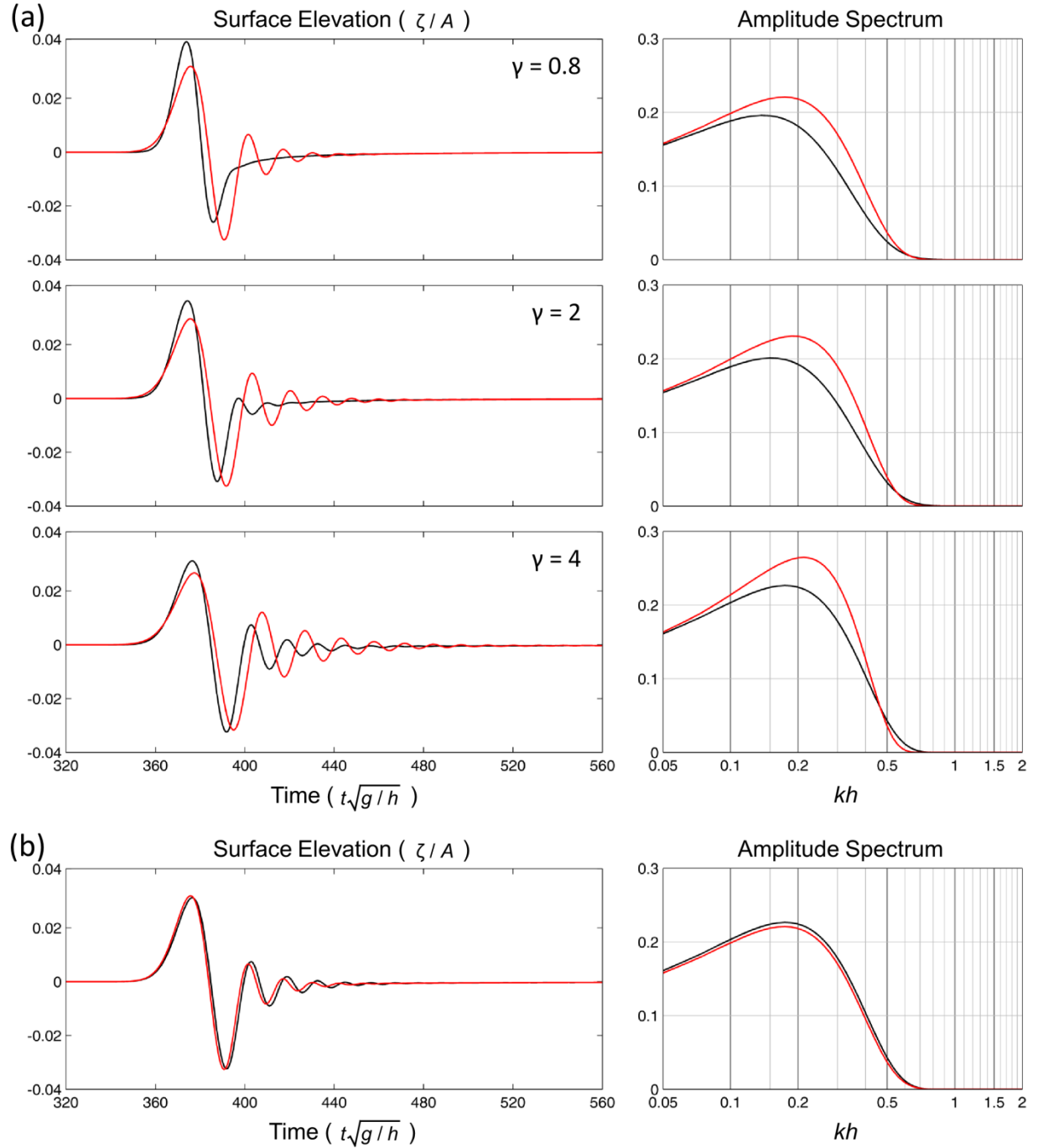


Figure 6. Time series and spectra at $x/h = 375$ along the axis resulting from a Gaussian hump with an effective diameter of $b/h = 30$ at the center of the computational grid. (a) Effects of the combined grid size and depth parameter γ . (b) Comparison of the hydrostatic and non-hydrostatic solutions with $\gamma = 4$ and 0.8 respectively. Black and red lines denote hydrostatic and non-hydrostatic solutions.

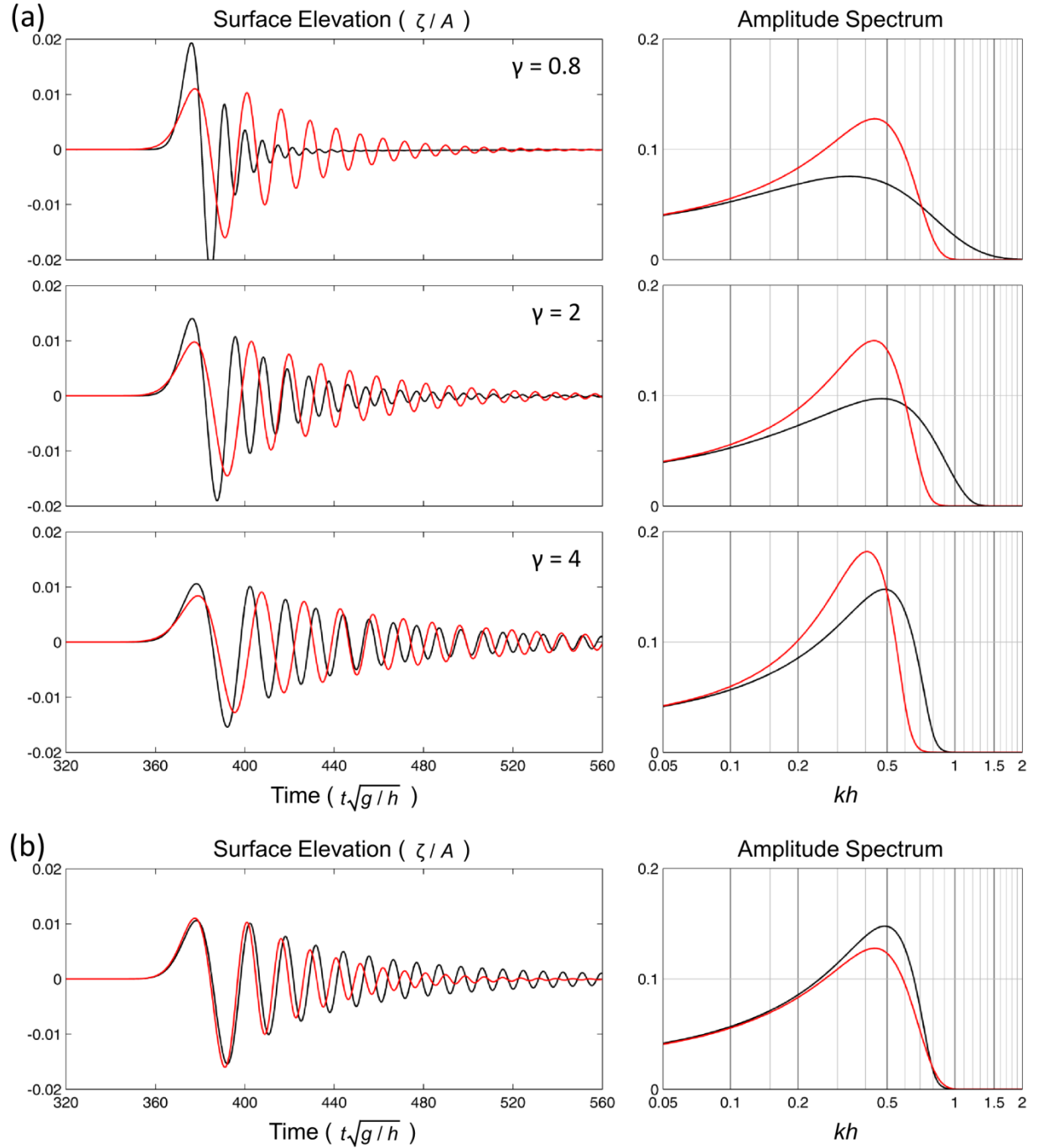


Figure 7. Time series and spectra at $x/h = 375$ along the axis resulting from a Gaussian hump with an effective diameter of $b/h = 15$ at the center of the computational grid. (a) Effects of the combined grid size and depth parameter γ . (b) Comparison of the hydrostatic and non-hydrostatic solutions with $\gamma = 4$ and 0.8 respectively. Black and red lines denote hydrostatic and non-hydrostatic solutions.

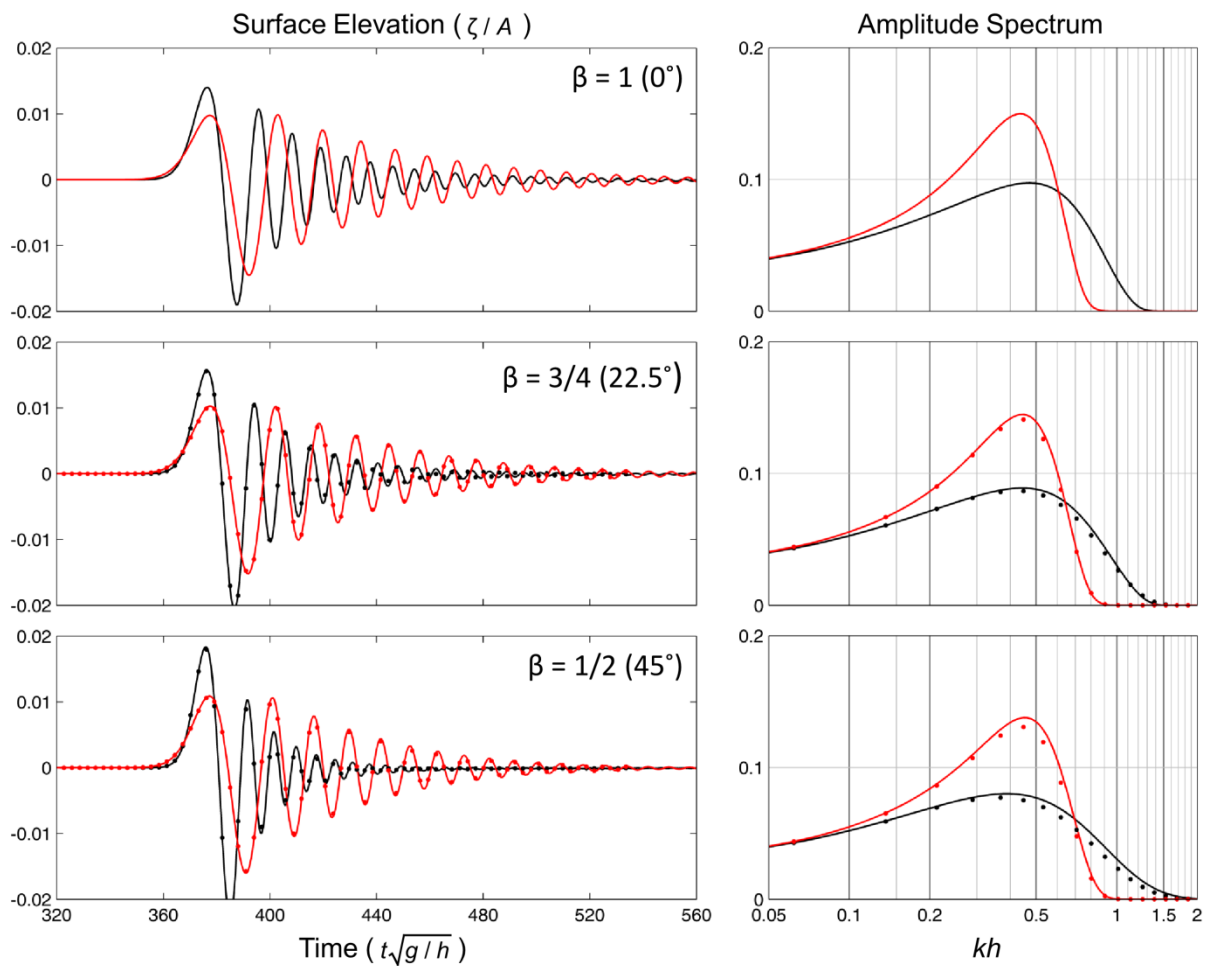


Figure 8. Time series and spectra at $r/h = 375$ from a Gaussian hump with an effective diameter of $b/h = 15$ at the center of the computational grid. Black and red lines indicate hydrostatic and non-hydrostatic solutions at 0° , 22.5° , and 45° oblique angles for $\gamma = 2$. Black and red dots denote hydrostatic and non-hydrostatic solutions obtained at the x axis using the effective grid spacing $\sqrt{\beta}\Delta x$ in separate numerical experiments.

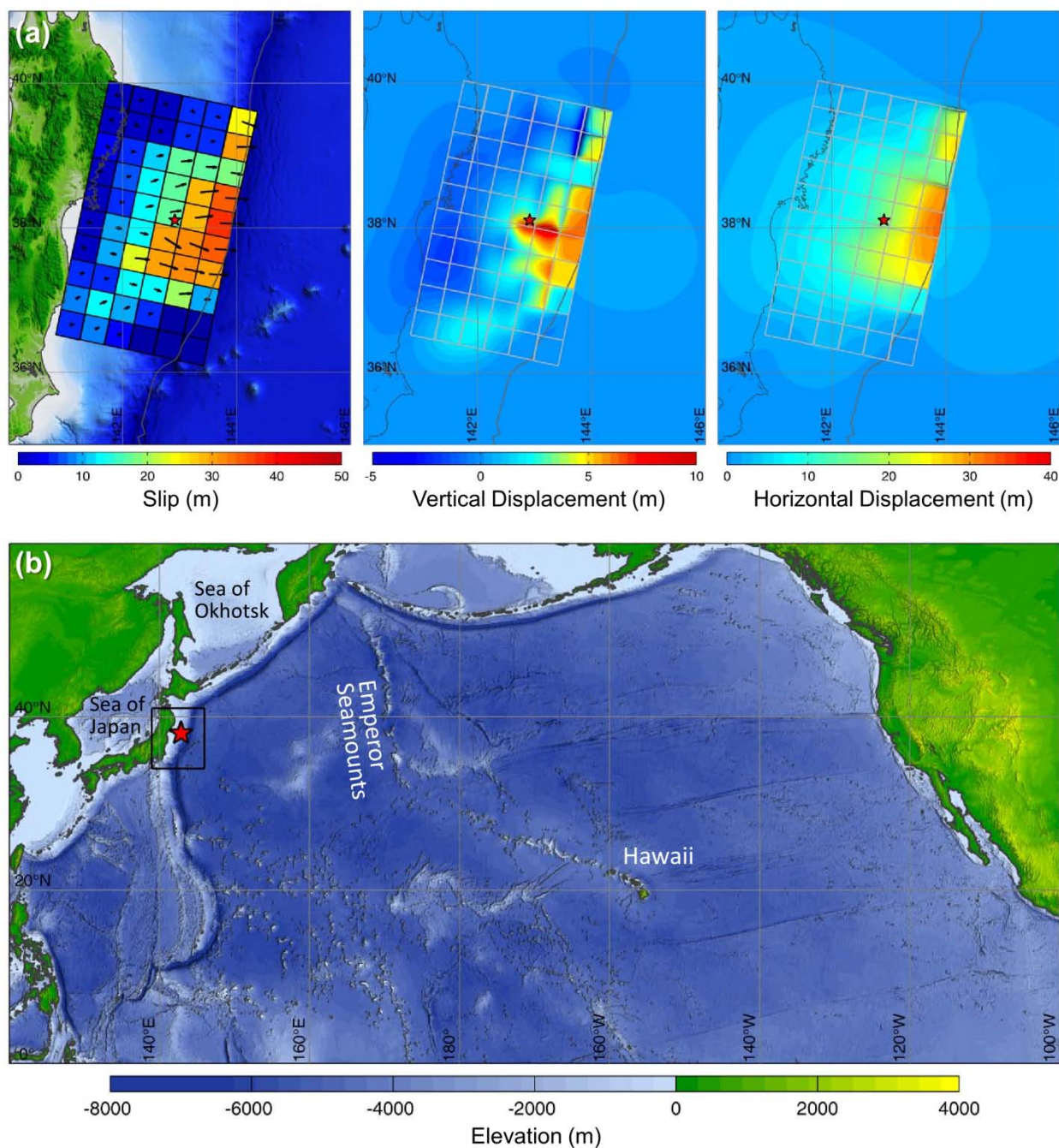


Figure 9. Tsunami excitation and computational grids. (a) Finite fault model and land surface displacement of the 2011 Tohoku earthquake from Yamazaki et al. (2018). (b) Computational domain and location map. Red star indicates the epicenter location and black rectangle delineates the nested grid.

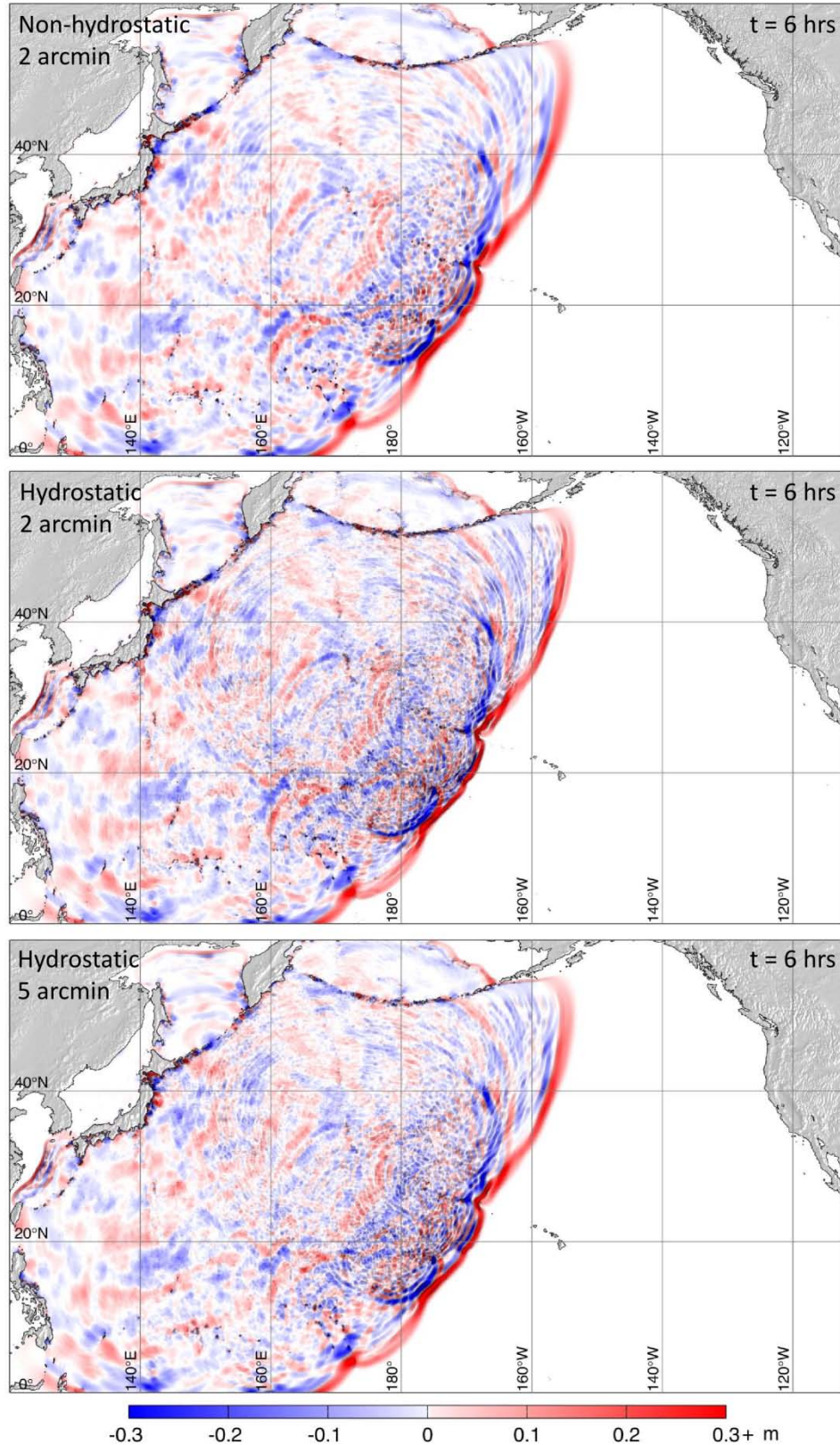


Figure 10. Surface elevations from non-hydrostatic and hydrostatic modeling of the 2011 Tohoku tsunami at prescribed grid sizes and 6 hours after the earthquake.

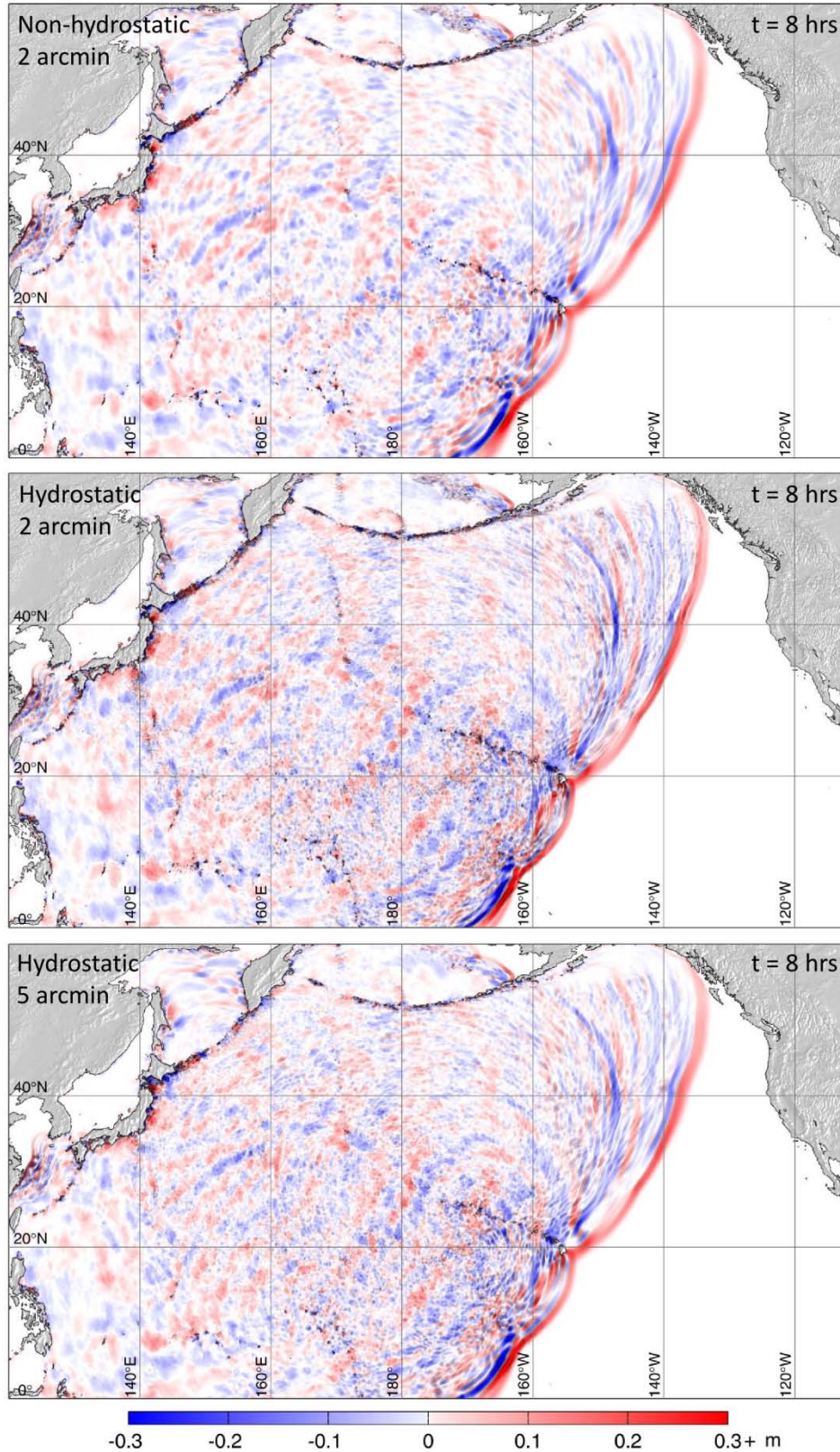


Figure 11. Surface elevations from non-hydrostatic and hydrostatic modeling of the 2011 Tohoku tsunami at prescribed grid sizes and 8 hours after the earthquake.

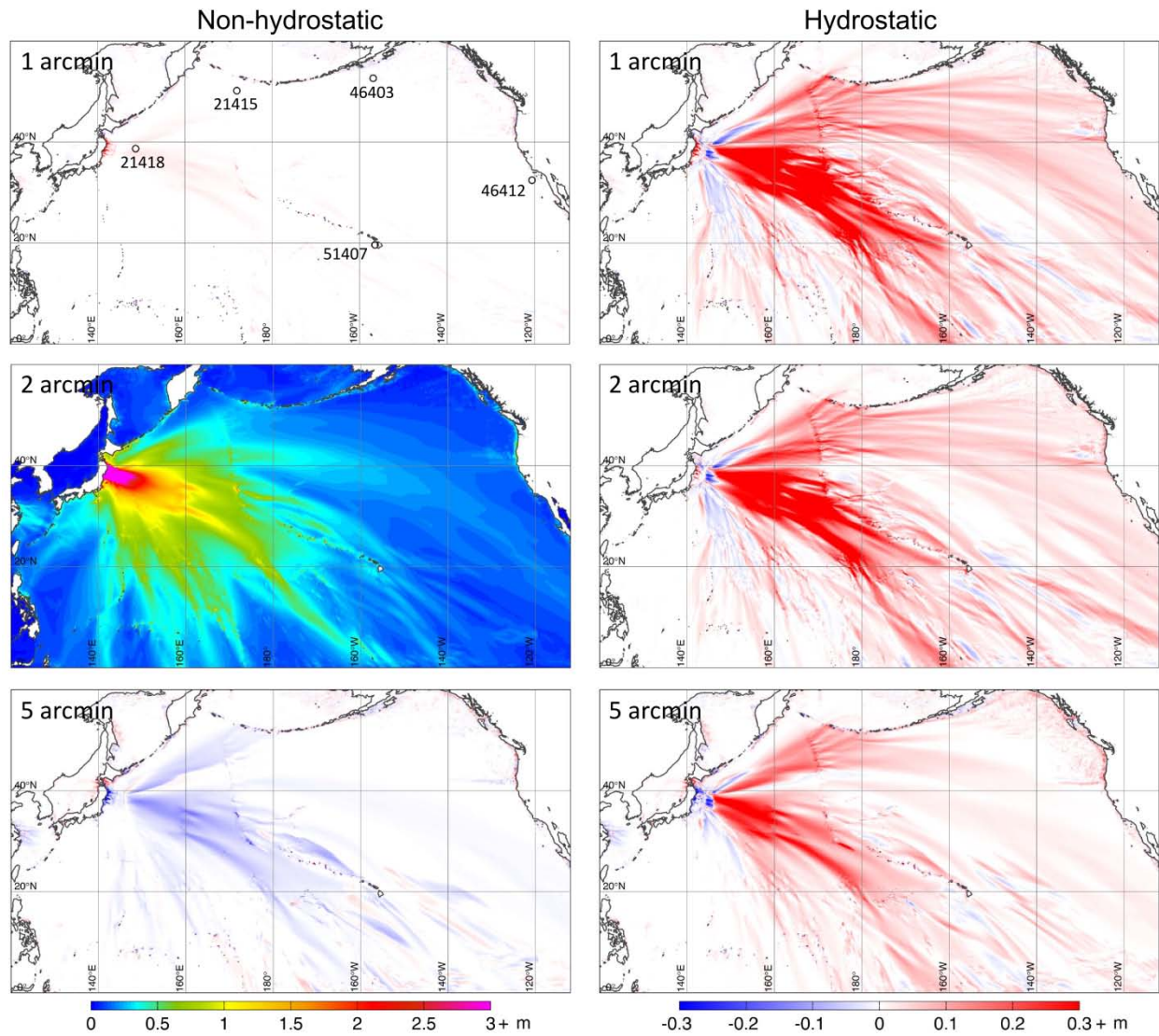


Figure 12. Reference wave amplitude based on the 2-arcmin non-hydrostatic solution (middle panel of left column) and its difference from non-hydrostatic (top and bottom panels of left column) and hydrostatic solutions (right column) at specified grid sizes. The continuous color palette denotes the reference wave amplitude. Red and blue in the two-tone color scheme indicate overestimation and underestimation of the reference wave amplitude. Open circles and labels in the top left panel indicate DART stations.

1082 Table 1. Initial peak amplitudes from non-hydrostatic and hydrostatic solutions normalized by
1083 observations of the 2011 Tohoku tsunami at selected DART stations.

DART	Observations (m)	Non-hydrostatic			Hydrostatic		
		1 arcmin	2 arcmin	5 arcmin	1 arcmin	2 arcmin	5 arcmin
21418	1.747	1.01	1.01	0.96	1.10	1.09	0.98
21415	0.264	0.96	0.93	0.86	1.38	1.37	1.34
46403	0.084	1.03	1.03	1.01	1.44	1.41	1.03
46412	0.120	0.91	0.91	0.87	1.14	1.06	0.95
51407	0.288	0.97	0.97	0.87	1.02	1.17	0.99

1084 Table 2. Initial peak arrival time from non-hydrostatic and hydrostatic solutions normalized by
1085 observations of the 2011 Tohoku tsunami at selected DART stations.

DART	Observations (hr:min)	Non-hydrostatic			Hydrostatic		
		1 arcmin	2 arcmin	5 arcmin	1 arcmin	2 arcmin	5 arcmin
21418	00:33	0.991	0.991	0.988	0.926	0.926	0.936
21415	03:11	1.010	1.005	1.005	0.990	0.990	0.995
46403	05:56	0.989	0.989	0.989	0.989	0.989	0.994
46412	10:22	0.989	0.989	0.989	0.987	0.984	0.986
51407	07:57	0.990	0.990	0.992	0.985	0.977	0.983

1086